Università degli Studi di Modena e Reggio Emilia

Dipartimento di Ingegneria "Enzo Ferrari"

Corso di Laurea Magistrale in Ingegneria del veicolo

Active control of Friction and Turbulent Heat Transfer at low Prandtl number

Relatore
Enrico Stalio

Correlatore
Filippo Moroni

Candidato
Daniele Tassinari
Matricola
191973

Anno Accademico 2025/2026

Abstract

This thesis investigates the effect of spanwise wall oscillations on convective heat transfer in turbulent flows at low Prandtl numbers. Direct Numerical Simulations (DNS) of fully developed turbulent channel flow are performed at a fixed friction Reynolds number of $Re_\tau = 180$. The temperature field is modelled using two passive scalars, solved simultaneously and characterized by the following Prandtl numbers: $Pr = 0.71$ (representative of air) and $Pr = 0.025$ (representative of liquid metals).
While spanwise forcing is a well-established active control technique for skin-friction drag reduction, its influence on thermal transport-particularly in the low-Prandtl-number regime, where the conductive sublayer extends significantly beyond the viscous sublayer-requires detailed investigation. The analysis focuses on evaluating the Heat-Transfer Reduction (HR) relative to Drag Reduction (DR).
The results indicate that for $Pr < 1$, the convective heat transfer is reduced less than the frictional drag (HR $<$ DR). This dissimilar behavior implies a breakdown of the Reynolds analogy, highlighting the potential of spanwise wall oscillations to achieve significant drag savings with a mitigated penalty on heat exchange efficiency in liquid metal applications.

Abstract in lingua italiana

L'obiettivo di questa tesi è investigare l'effetto delle oscillazioni trasversali della parete sullo scambio termico convettivo in regime turbolento a bassi numeri di Prandtl. Sono state condotte delle Simulazioni Numeriche Dirette (DNS) di un canale piano turbolento completamente sviluppato ad un numero di Reynolds di attrito fissato a $Re_\tau = 180$. La temperatura è modellata come due scalari passivi calcolati simultaneamente caratterizzati dai seguenti numeri di Prandtl: $Pr = 0.71$ (tipico dell'aria) e $Pr = 0.025$ (tipico dei metalli liquidi).
Sebbene il forzamento trasversale sia una tecnica di controllo attivo consolidata per la riduzione della resistenza d'attrito, la sua influenza sul trasporto termico - particolarmente a bassi numeri di Prandtl, dove il sottostrato conduttivo si estende ben oltre quello viscoso - richiede un'indagine dettagliata. L'analisi si concentra sulla valutazione della riduzione dello scambio termico (HR) rispetto alla riduzione della resistenza d'attrito (DR).
I risultati indicano che per $Pr < 1$, lo scambio termico convettivo si riduce in misura minore rispetto all'attrito (HR $<$ DR). Questo comportamento dissimile implica una rottura dell'analogia di Reynolds, evidenziando il potenziale delle oscillazioni trasversali nell'ottenere un notevole risparmio energetico legato all'attrito con una penalizzazione ridotta sull'efficienza dello scambio termico nelle applicazioni con metalli liquidi.

Contents

Nomenclature

Roman Symbols

A Amplitude of wall oscillation

A_{fact} Reynolds analogy factor

c Specific heat capacity at constant pressure

C_f Skin friction coefficient

DR Drag reduction

h Half channel height

h_{conv} Convective heat transfer coefficient

HR Heat transfer reduction

Nu Nusselt number

p Instantaneous pressure

P Mean pressure

p^* Periodic residual of the pressure field

Pr Prandtl number

q_i Mean scalar flux vector

q_w Wall heat flux

Q Volumetric heat source

Re Reynolds number

Re_b Bulk Reynolds number

Re_τ Friction Reynolds number

Sc Schmidt number

St Stanton number

t Time

T Temperature

T_b Bulk temperature

U_b Bulk velocity

u_i, u, v, w Instantaneous velocity components

U_i, U, V, W Mean velocity components

u_i', u', v', w' Fluctuating velocity components

u_τ Friction velocity

U_p Reference characteristic velocity

w_w Wall velocity

x_i, x, y, z Spatial coordinates (streamwise, wall-normal, spanwise)

Greek Symbols

α Thermal diffusivity

δ_ν Viscous length scale

λ Thermal conductivity

μ Dynamic viscosity

ν Kinematic viscosity

ρ Fluid density

τ Total shear stress

τ_w Wall shear stress

ϕ Passive scalar

Φ Mean passive scalar

ϕ' Fluctuating passive scalar

ϕ_τ Friction temperature

ω Angular frequency of wall oscillation

Subscripts and Superscripts

$(\cdot)^+$ Quantity scaled in viscous (inner) wall units

$(\cdot)_b$ Bulk quantity

$(\cdot)_w$ Wall quantity

$\langle\cdot\rangle$ Averaged quantity

List of Figures

List of Tables

Introduction

The efficiency of thermal-hydraulic systems is a critical constraint in modern engineering, with critical applications in heat exchangers, gas turbines, and cooling systems for advanced nuclear reactors (Incropera (2017) [1]; Forsberg (2021) [2]). In many high-performance industrial environments, the use of working fluids with extremely low molecular Prandtl number ($Pr \ll 1$), such as liquid metals, requires an in-depth understanding of turbulent scalar transport. Unlike conventional fluids like air or water, where the thermal and momentum boundary layers are of comparable thickness, liquid metals exhibit a thermal sublayer that extends significantly beyond the viscous one, fundamentally altering the interplay between velocity and temperature fields (Tiselj (2014) [15]).
Turbulent heat transport has been traditionally governed by the Reynolds analogy, which postulates a direct proportionality between momentum and heat transfer (Stephen B. Pope (2000) [10]). This conceptual framework, while robust in predicting scalar transport at $Pr \approx 1$ (Kim & Moin (1989) [8]; Kasagi (1992) [7]), acts as a design bottleneck in engineering applications: techniques developed to reduce the skin-friction drag often lead to a proportional degradation of heat transfer efficiency. The structural correlation between velocity and temperature fields in the wall region has been widely investigated by Stalio & Nobile (2003) [14], confirming that the turbulent transport of scalars is inherently coupled to the coherent structures of the velocity field.
However, the mathematical divergence between the solenoidal nature of the velocity field and the conservative nature of the scalar field enables the concept of dissimilar control (Hasegawa & Kasagi (2011) [5]). Among active control strategies, spanwise wall forcing, such as spanwise wall oscillations (SWO), has emerged as a highly effective method for disrupting near-wall coherent structures, such as streaks and quasi-streamwise vortices (Quadrio & Ricco (2011) [11] ; Ricco (2012) [12]).
The potential for "breaking" the Reynolds analogyhas recently attracted considerable attention. Studies by Guérin et al. 2024 [4] and Rouhi et al. 2025 [13] have demonstrated that, under specific forcing parameters, it is possible to achieve a preferential enhancement of heat transfer over drag, challenging the classical paradigm of coupled transport. Yet, these advancements have predominantly focused on fluids with $Pr \geq 1$. In the low-Prandtl regime, the thermal field's sensitivity to large-scale turbulent motions renders it less responsive to near-wall modifications that typically characterize high-Prandtl number fluids. Consequently, the effect of the active control on scalar transport in liquid metals remains a critical unresolved research question, as previously noted in specialized MSc work by Galli et al. 2023 [3].
This thesis aims to bridge this gap by investigating the thermal response of a tur-

bulent channel flow to spanwise wall oscillations via Direct Numerical Simulations (DNS). The study is conducted at a friction Reynolds number of $Re_\tau = 180$. A key feature of the present work is the simultaneous calculation of two passive scalars, characterized by $Pr = 0.71$ and $Pr = 0.025$. By quantifying the divergence between drag reduction (DR) and heat transfer reduction (HR) for both Prandtl numbers, this work evaluates whether the Stokes layer induced by spanwise forcing can be leveraged to optimize thermal performance in high-efficiency industrial systems, extending the existing findings into the realm of liquid metal cooling.

Chapter 1

Wall turbulence

This chapter provides a brief introduction to the governing equations of fluid flow and a description of turbulent channel flow.

1.1 Governing Equations

The governing equations of an incompressible flow are the Navier–Stokes equations, which consist of the continuity equation (mass conservation) and the momentum equations.

$$\frac{\partial u_i}{\partial x_i} = 0 \tag{1.1}$$

$$\frac{\partial u_i}{\partial t} + \frac{\partial (u_i u_j)}{\partial x_j} = -\frac{1}{\rho}\frac{\partial p}{\partial x_i} + \nu \frac{\partial^2 u_i}{\partial x_j \partial x_j} \tag{1.2}$$

where u_i are the velocity components, p is the pressure, x_i are the Cartesian coordinates, and ν is the kinematic viscosity. The index $i = x, y, z$ denotes the spatial directions.

The Navier–Stokes equations express the conservation of mass and momentum for a Newtonian fluid. In particular, the momentum equation represents a balance between inertial forces, pressure forces, and viscous stresses. The nonlinear convective term plays a crucial role, as it governs the transfer of momentum across the flow and is responsible for the development of instabilities.

In the study of turbulent flows, it is customary to introduce a statistical description based on the Reynolds decomposition. Any flow quantity can be decomposed into a mean component and a fluctuating component. For the velocity field:

$$u_i(x, y, z, t) = U_i(x, y, z) + u_i'(x, y, z, t) \tag{1.3}$$

where $U_i = \langle u_i \rangle$ denotes the mean velocity field obtained through an appropriate averaging operation (e.g., time or ensemble average), and u_i' represents the fluctuating component. By definition of the averaging operator, the fluctuating component satisfies $\langle u_i' \rangle = 0$. Under the assumption of statistical stationarity, the mean velocity field does not depend on time, which simplifies the analysis of turbulent flows.

Introducing the Reynolds decomposition into the Eqs. (1.1) and (1.2) and applying the averaging operator yields:

$$\frac{\partial U_i}{\partial x_i} = 0 \tag{1.4}$$

$$\frac{\partial U_i}{\partial t} + \frac{\partial (U_i U_j)}{\partial x_j} = -\frac{1}{\rho}\frac{\partial P}{\partial x_i} + \nu \frac{\partial^2 U_i}{\partial x_j \partial x_j} - \frac{\partial \langle u_i' u_j' \rangle}{\partial x_j} \tag{1.5}$$

The term $\langle u_i' u_j' \rangle$ represents the Reynolds stress tensor, which arises from the non-linear interaction between the fluctuating velocity components after applying the averaging operator. These equations cannot be solved directly because the Reynolds stress tensor introduces additional unknowns, leading to the turbulence closure problem. Specifically, the symmetric Reynolds stress tensor introduces six additional independent unknowns that require appropriate closure models.

1.2 Channel flow

Turbulent channel flow represents one of the canonical configurations of wall-bounded turbulent flows and is widely used as a canonical case for theoretical and numerical investigations.

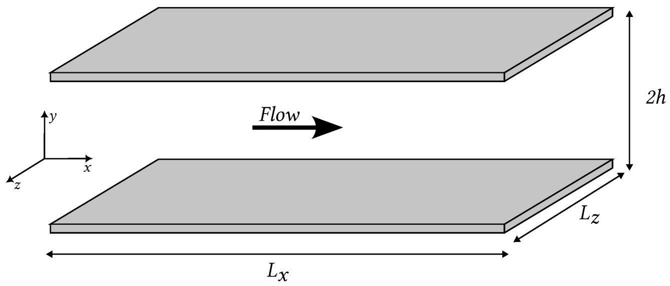

Figure 1.1: Channel flow geometry.

The geometry consists of two infinite parallel walls separated by a distance $2h$. The streamwise, wall-normal, and spanwise directions are denoted by x, y, and z, respectively.
The flow regime is commonly characterized by the Reynolds number, that is a dimensionless parameter defined as:

$$Re = \frac{U_{ref} h}{\nu} \tag{1.6}$$

where U_{ref} is a reference velocity, which in the case of channel flow is the bulk velocity U_b defined as:

$$U_b = \frac{1}{2h} \int_0^{2h} \langle u \rangle dy \tag{1.7}$$

Although the exact transition depends on disturbances and inlet conditions, laminar flow is typically observed for sufficiently low Reynolds numbers ($Re < 2000$), whereas turbulence is sustained at sufficiently high Reynolds numbers ($Re > 4000$).

In turbulent channel flow, the statistical description of the flow is introduced through the Reynolds decomposition. Under this framework, the governing equations can be simplified by considering the following assumptions:

- The flow is statistically steady, meaning all statistical quantities are independent of time $\left(\frac{\partial\langle\cdot\rangle}{\partial t}=0\right)$.
- The flow is fully developed, meaning statistical quantities do not depend on the streamwise direction x $\left(\frac{\partial\langle\cdot\rangle}{\partial x}=0\right)$.
- The flow is homogeneous in the spanwise direction z.
- The flow is driven by a constant pressure gradient in the streamwise direction $\left(\frac{\partial P}{\partial x}\neq 0\right)$.

Under these assumptions, the mean velocity field reduces to:

$$U=U(y),\quad V=0,\quad W=0 \tag{1.8}$$

The mean continuity equation is:

$$\frac{\partial U}{\partial x}+\frac{\partial V}{\partial y}+\frac{\partial W}{\partial z}=0 \tag{1.9}$$

By applying the assumptions of homogeneity in x and z, it reduces to:

$$\frac{\partial V}{\partial y}=0 \tag{1.10}$$

which implies that V is constant. By imposing the no-penetration boundary condition at the wall ($V=0$), it follows that $V(y)=0$ everywhere in the channel. Applying the previous assumptions to the Eq. (1.5) in the wall-normal direction reduces to:

$$\frac{1}{\rho}\frac{\partial P}{\partial y}=-\frac{d\langle v'^2\rangle}{dy} \tag{1.11}$$

Integrating with respect to y, one obtains:

$$\frac{1}{\rho}P(x,y)-\frac{1}{\rho}P_w(x)=-\langle v'^2\rangle \tag{1.12}$$

Since the right-hand side depends only on y, differentiating with respect to x yields:

$$\frac{\partial P}{\partial x}(x,y)=\frac{dP_w}{dx} \tag{1.13}$$

i.e., the streamwise pressure gradient is independent of the wall-normal coordinate. Similarly, the mean momentum equation in the streamwise direction reduces to:

$$0=-\frac{1}{\rho}\frac{dP_w}{dx}+\nu\frac{d^2U}{dy^2}-\frac{d\langle u'v'\rangle}{dy} \tag{1.14}$$

This equation expresses the balance between the driving force due to the imposed pressure gradient, the viscous stress, and the turbulent momentum transport.
It is convenient to introduce the total shear stress

$$\tau = \mu \frac{\partial U}{\partial y} - \rho \langle u'v' \rangle \tag{1.15}$$

so the momentum equation can be rewritten as:

$$\frac{d\tau}{dy} = \frac{dP_w}{dx} \tag{1.16}$$

Since $\tau = \tau(y)$ and $P_w = P_w(x)$, the only solution compatible with the above balance is:

$$\frac{d\tau}{dy} = \frac{dP_w}{dx} = \text{constant} \tag{1.17}$$

Integrating in the wall-normal direction:

$$\tau(y) - \tau_w = y \frac{dP_w}{dx} \tag{1.18}$$

where $\tau_w = \tau(0)$ is the wall shear stress. By symmetry, the total shear stress vanishes at the channel centerline ($\tau(h) = 0$), which leads to $\tau_w = -h\frac{dP_w}{dx}$. Substituting into the previous expression:

$$\tau(y) = \tau_w \left(1 - \frac{y}{h}\right) \tag{1.19}$$

where τ_w is the wall shear stress. The total shear stress represents the flux of streamwise momentum toward the wall. This flux is composed of a viscous contribution ($\mu\frac{dU}{dy}$), dominant in the near-wall region, and a turbulent contribution ($-\rho\langle u'v' \rangle$), dominant away from the wall.
To quantify the wall shear stress, which the flow exerts on the wall, it is convenient to introduce the *skin-friction coefficient* defined as:

$$C_f = \frac{\tau_w}{\frac{1}{2}\rho U_{ref}^2} \tag{1.20}$$

where U_{ref} is a reference velocity, which in the case of channel flow is the bulk velocity U_b.

1.3 Universal scaling of wall turbulence

As derived in the previous section Eq. (1.19), the total shear stress varies linearly across the channel. To obtain a universal representation of the mean flow profile, it is necessary to define the relevant scales. By utilizing the wall shear stress τ_w and the fluid density ρ, the characteristic velocity scale known as the *friction velocity* u_τ can be defined as:

$$u_\tau = \sqrt{\frac{\tau_w}{\rho}} \tag{1.21}$$

Consequently, the characteristic length scale or *viscous length* δ_ν is given by:

$$\delta_\nu = \frac{\nu}{u_\tau} \tag{1.22}$$

Using these friction units, a characteristic parameter known as the *friction Reynolds number* Re_τ can be introduced:

$$Re_\tau = \frac{u_\tau h}{\nu} = \frac{h}{\delta_\nu} \tag{1.23}$$

This parameter expresses the ratio between the global geometrical length scale, thereby providing a direct measure of the scale separation between the largest outer structures and the smallest dissipative eddies within the flow.
The wall-normal distance measured in friction units is defined as:

$$y^+ = \frac{y}{\delta_\nu} = \frac{y u_\tau}{\nu} \tag{1.24}$$

This non-dimensional distance can be interpreted as a local Reynolds number that quantifies the relative importance of turbulent and viscous momentum transport. Observing different behavior in different regions:

- *Near-wall asymptotic* ($Re_\tau \gg 1$ and $y/h \ll 1$): where the viscous contibution is the 100% of the total shear stress.
- *Outer asymptotic* ($Re_\tau \gg 1$ and $y/h \approx 1$): where all the streamwise momentum transport is carried by the Reynolds stresses, viscous diffusion is negligible.
- *Overlap layer asymptotic* ($Re_\tau \gg 1$ and $y/h \ll 1$): a matching region where both viscous and turbulent stress gradients play a role, bridging the inner near-wall region and the outer core flow.

1.4 Mean velocity profile

The mean velocity profile in wall turbulence can be described by the *law of the wall.* In the inner layer ($y/h \ll 1$), the mean velocity profile is determined solely by the viscous scales, independently of the outer length scale h. This leads to the *inner scaling*:

$$U^+ = f(y^+) \tag{1.25}$$

where $U^+ = U/u_\tau$ is the non-dimensional mean velocity.
In the near wall region (viscous sub-layer) ($y^+ < 5$), the Reynolds shear stress is negligible compared with the viscous stress. A Taylor-series expansion of the law of the wall yields the linear relation:

$$U^+ = y^+ \tag{1.26}$$

In the outer part of inner layer (log-law region) ($y^+ > 30$ and $y/h < 0.3$) where $y/\delta \ll 1$ and $y^+ \gg 1$, viscous effects become negligible. Under this condition, the velocity gradient function approaches as a constant, so the logarithmic law of the wall is obtained:

$$U^+ = \frac{1}{\kappa}\ln(y^+) + B \tag{1.27}$$

where $\kappa \approx 0.41$ is the von Kármán constant and $B \approx 5.2$ is an additive constant.
The buffer layer ($5 < y^+ < 30$) represents the transitional zone between the viscosity-dominated viscous sublayer and the turbulence-dominated log-law region, where neither the linear law nor the log law holds exactly.

1.5 Coherent structures in wall turbulence

Turbulent flows are characterized by complex, multi-scale motions that can be classified into more elementary components known as coherent turbulent structures. These structures are defined as regions of space containing organized motions whose features are phase-correlated over the entire spatial extent of the structure, and their dynamics can be explained through fundamental mechanical arguments.
The main features of coherent structures include:

- *Large-scale organized motions*;
- *High rates of momentum transport and scalar mixing.*

For these reasons, coherent structures are the primary target in the development of active and passive flow control devices aimed at optimizing the aerodynamic or thermal performance of the system under consideration.
Prominent examples of coherent structures in wall-bounded turbulence are:

- *Quasi-streamwise vortices:* Counter-rotating vortical structures elongated in the flow direction, responsible for pumping fluid away from or toward the wall.
- *Streamwise velocity streaks:* Alternating regions of high- and low-speed fluid generated in the viscous sublayer by the action of the vortices.

In wall turbulence, these structures are strictly coupled and form a non-linear *self-sustaining cycle*: the quasi-streamwise vortices generate the velocity streaks through advection, and the streaks eventually become unstable, break down, and generate new vortices. Manipulating or disrupting this specific cycle is the key mechanism used by active control strategies to achieve drag reduction and modulate heat transfer.

Chapter 2

Passive scalar mixing and Heat transfer

A scalar is a quantity defined by a single value at each point in space. This chapter focuses on the turbulent transport of chemical or thermal species characterized solely by their concentration or temperature field. In this framework, the scalar field is uniquely described by its local intensity.
The scalar is referred to as *passive* because it is dynamically inactive; it is simply transported by the velocity field, while its evolution does not exert any feedback force on the fluid motion or the turbulence dynamics. This fundamental assumption implies that the scalar satisfies the following physical conditions:

- the species is chemically inert, i.e. no reactions occur due to concentration variations;
- surface tension effects are neglected;
- the scalar is neutrally buoyant, meaning that the transported substance has the same density as the carrier fluid;
- the scalar does not significantly affect the fluid density or viscosity, as in the case of small temperature variations.

2.1 Behavior of a passive scalar

Laminar condition: Consider a laminar boundary layer over a wall featuring a constant passive scalar source (e.g., a heated wall where the scalar represents temperature). As the flow develops downstream, the scalar field is governed by two concurrent phenomena: advection and molecular diffusion. Fluid particles are transported downstream by the velocity field while thermal or molecular diffusion acts perpendicular to the bulk motion. This diffusion causes the scalar boundary layer thickness to grow.
The fundamental role of molecular diffusion is to smooth out the scalar concentration gradients. Moving downstream, the same scalar concentration difference ΔT occurs over a progressively larger distance; therefore, the only physical mechanism

capable of increasing the volume of fluid characterized by a certain scalar concentration is the diffusion of the scalar itself. The diffusive flux is defined as $\alpha\nabla\phi$, where α is the diffusion coefficient and $\nabla\phi$ is the gradient of the passive scalar. Further downstream, the local scalar diffusion decreases due to the progressive reduction of the concentration gradient. Ultimately, while the scalar field is subjected to both advection and diffusion, the growth of the thermal boundary layer thickness is strictly governed by diffusion rather than bulk fluid motion.
Turbulent condition: In a turbulent regime, while advection and molecular diffusion remain active, the transport mechanism is radically altered by turbulent fluctuations, leading to a massive enhancement in scalar mixing. Within a turbulent boundary layer, a wide spectrum of eddy scales continuously distorts, stretches, and folds the scalar field.
In conventional turbulent flows (where the diffusivity is of the same order as the viscosity), this turbulent motion effectively homogenizes the scalar concentration within the core flow, resulting in a nearly uniform distribution. Consequently, the role of turbulence can be summarized as follows:

- It drastically increases the interfacial area between regions of different scalar concentrations, enhancing the overall rate of molecular diffusion;
- It reduces the local mixing length scales, generating steeper scalar gradients over highly convoluted surfaces.

However, it is worth noting that this structural behavior is strongly dependent on the fluid properties, particularly when molecular thermal diffusion significantly outpaces momentum diffusion.

2.2 Passive scalar equation

This equation governs the evolution of a passive scalar through advection and diffusion. it is defined as:

$$\frac{\partial\phi}{\partial t} + u_i\frac{\partial\phi}{\partial x_i} = \alpha\frac{\partial^2\phi}{\partial x_i\partial x_i} \tag{2.1}$$

where ϕ is the passive scalar, u_i is the velocity component in the $i = x, y, z$ direction and α is the coefficient of diffusion. This equation is simpler than the Navier–Stokes equations because the advective term is linear and the velocity field is not coupled with the pressure field.
Nevertheless, the passive scalar still exhibits non-trivial behaviour. The relative importance of molecular scalar diffusion with respect to momentum diffusion is commonly quantified by the Schmidt number, defined as:

$$Sc = \frac{\nu}{\alpha} \tag{2.2}$$

where ν is the kinematic viscosity. When the passive scalar represents a temperature field, the Schmidt number is equivalently designated as the Prandtl number (Pr), where α specifically denotes the thermal diffusivity:

$$\alpha = \frac{\lambda}{\rho c} \tag{2.3}$$

Due to the chaotic nature of turbulent transport, a statistical approach is required. Applying the Reynolds decomposition, the instantaneous scalar field is split into a mean and a fluctuating component:

$$\phi(x, y, z, t) = \Phi(x, y, z) + \phi'(x, y, z, t) \tag{2.4}$$

where $\Phi = \langle\phi\rangle$ is the ensemble or time average ($\langle\phi'\rangle = 0$). Substituting this decomposition into the governing equation and averaging yields the mean passive scalar equation:

$$\frac{\partial\Phi}{\partial t} + U_i\frac{\partial\Phi}{\partial x_i} = \alpha\frac{\partial^2\Phi}{\partial x_i\partial x_i} - \frac{\partial\langle\phi' u_i'\rangle}{\partial x_i} \tag{2.5}$$

The term $\langle\phi' u_i'\rangle$ represents the turbulent scalar flux tensor, which embodies the transport of scalar fluctuations by velocity fluctuations. This introduces the classic turbulence closure problem for scalars, as Eq. (2.5) introduces three new unknowns. Analogous to the total shear stress, the total mean scalar flux vector q_i can be defined as the sum of molecular and turbulent contributions:

$$q_i = -\alpha\frac{\partial\Phi}{\partial x_i} + \langle\phi' u_i'\rangle \tag{2.6}$$

2.3 Passive scalar in wall turbulence

Consider a turbulent channel flow configuration under the assumptions introduced in the previous chapter:

- The flow is statistically steady;
- The flow is fully developed;
- The flow is homogeneous in the spanwise direction.

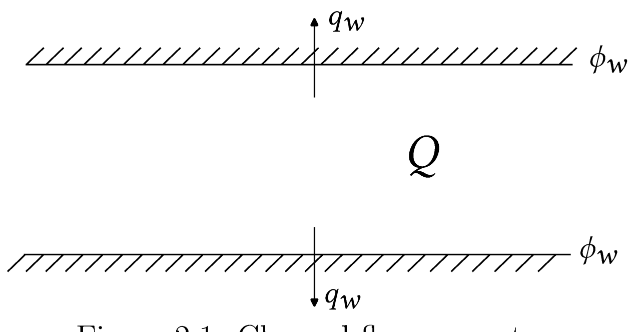

Figure 2.1: Channel flow geometry.

From this point forward, the passive scalar is explicitly treated as a thermal field and the scalar variable is defined as $\phi = \rho cT$ (with T being the temperature, ρ the fluid density, and c the specific heat capacity). Both walls are maintained at the same fixed temperature ϕ_w. Inside the channel there is a volumetric source of heat Q that is homogeneous. This term plays a role analogous to the imposed pressure gradient in the momentum equation, as it continously supplies thermal energy to the flow. As a consequence, a wall-normal heat-flux q_w is established toward the channel walls. The temperature field can also be decomposed into a mean and a fluctuating component:

$$T = T_m + T' \tag{2.7}$$

Substituting the Eq. (2.7) into the Eq. (2.6) remembering that $\Phi = \rho c T_m$ and $\phi' = \rho c T'$ yields:

$$q_i = -\alpha \rho c \frac{\partial T_m}{\partial x_i} + \rho c \langle T' u_i' \rangle \tag{2.8}$$

Introducing the Eq. (2.7) into the Eq. (2.5) yields:

$$\rho c \frac{\partial T_m}{\partial t} + \rho c \frac{\partial (T_m U_i)}{\partial x_i} = \alpha \rho c \frac{\partial^2 T_m}{\partial x_i \partial x_i} - \rho c \frac{\partial \langle T' u_i' \rangle}{\partial x_i} + Q \tag{2.9}$$

where Q represents the volumetric source of heat, which in general is a function of space and time. Applying the channel flow simplifications to the averaged energy equation yields the steady-state balance:

$$0 = \alpha \frac{d^2 T_m}{dy^2} - \frac{d \langle T' u_y' \rangle}{dy} + \frac{Q}{\rho c} \tag{2.10}$$

Multiplying by ρc, this balance can be compactly written as the derivative of the total heat flux:

$$\frac{dq_y}{dy} = Q \tag{2.11}$$

Integrating from the bottom wall ($y = 0$) up to a generic wall-normal position y yields:

$$q_y - q_w = Qy \tag{2.12}$$

where $q_w = q_y(0)$ is the wall heat flux. Due to the geometric symmetry of the channel, the total heat flux must vanish at the centerline ($q_y(h) = 0$), which uniquely dictates the required strength of the volumetric source:

$$Q = -\frac{q_w}{h} \tag{2.13}$$

Substituting this relation back into the integrated balance gives:

$$q_y(y) = q_w \left(1 - \frac{y}{h}\right) \tag{2.14}$$

This last equation proves that the total heat flux varies perfectly linearly across the channel half-height, demonstrating a rigorous mathematical analogy to the total shear stress profile Eq. (1.19).In the near-wall region, heat transfer is dominated by molecular conduction (the conductive sublayer), whereas turbulent convective transport $\rho c \langle T' u_y' \rangle$ becomes dominant throughout the core flow.

2.4 Universal scaling of passive scalar

To achieve a universal description of the mean temperature profile independent of the specific Reynolds number, non-dimensional friction scales must be introduced. By employing the friction velocity u_τ defined in Eq. (1.21) and the wall heat flux, a characteristic reference scale known as the friction temperature ϕ_τ can be defined as:

$$\phi_\tau = \frac{q_w}{\rho c u_\tau} = \frac{\lambda}{\rho c u_\tau} \left| \frac{\partial \phi}{\partial y} \right|_{y=0} = \frac{\alpha}{u_\tau} \left| \frac{\partial \phi}{\partial y} \right|_{y=0} \tag{2.15}$$

Another important reference scale is the *diffusion length* l_α, is defined as:

$$l_\alpha = \frac{\alpha}{u_\tau} \tag{2.16}$$

Using Eq. (2.15) it is possible to define the non-dimensional mean scalar profile as:

$$\Phi^+ = \frac{\Phi - \Phi_w}{\phi_\tau} \tag{2.17}$$

By doing the same reasoning as for the mean velocity profile, it is possible to define the following asymptotic regions:

- *Near wall region* ($y/l_\alpha < 5$): Where the behavior of the mean passive scalar is the same of the mean velocity profile, but only in case of $Pr = 1$, so when the diffusion coefficient of the scalar is equal to the viscosity.

- *Overlap layer* ($y/l_\alpha \gg 1$ and $y/h \ll 1$): Far enough from the wall for viscous and conductive effects to be negligible, yet close enough for the wall-normal coordinate to restrict eddy sizes. In this layer, the mean temperature follows a logarithmic distribution:

$$\Phi^+ = \frac{1}{\kappa_\phi} \ln\left(\frac{y}{l_\alpha}\right) + B_\phi \tag{2.18}$$

  where κ_ϕ is the von Kármán constant for the scalar field and B_ϕ is an additive constant.

2.5 Prandtl Number Effects

The Prandtl number quantifies the relative importance of momentum and scalar diffusion. If $Pr = 1$, the mean temperature profile is linear for $y^+ < 5$, but if the Prandtl number is different from unity, the linear behavior of the mean temperature profile remains valid over a shorter distance.
For $Pr > 1$, the conductive range shrinks because the kinematic viscosity is larger than the thermal diffusivity ($\nu > \alpha$). Conversely, for $Pr < 1$, the conductive range expands because the kinematic viscosity is smaller than the thermal diffusivity ($\nu < \alpha$). The smaller scales of the scalar field depend on the Prandtl number; specifically, the smaller the diffusivity of the scalar, the smaller the scales of the scalar field become.
In the logarithmic overlap region, the slope of the mean temperature profile does not change with the Prandtl number, whereas the shift does:

- If $Pr = 1$: The shift is zero, and the mean temperature profile matches the mean velocity profile;
- If $Pr > 1$: An upward shift of the mean temperature profile is observed;
- If $Pr < 1$: A downward shift of the mean temperature profile is observed.

Consequently, when the Prandtl number is high, the diffusivity is smaller than the viscosity of the fluid, and therefore the conductive range becomes thinner. The opposite behavior occurs for small Prandtl numbers.

2.6 Heat transfer parameters

To evaluate the efficiency of the thermal transport, it is useful to introduce dimensionless parameters. The Stanton number (St) represents the non-dimensional heat transfer coefficient and serves as the thermal counterpart to the skin-friction coefficient C_f. It is defined as:

$$St = \frac{q_w}{\rho c U_{ref}(T_w - T_{ref})} \tag{2.19}$$

where the reference temperature T_{ref} in the case of channel flow is the bulk tepera- ture T_b defined as:

$$T_b = \frac{1}{2hU_b} \int_0^{2h} \langle uT \rangle dy \tag{2.20}$$

By definition of wall heat flux $q_w = \lambda \left.\frac{d\Phi}{dy}\right|_{y=0}$, and that $\lambda = \alpha \rho c$ and recalling the Eq. (2.15) it possible write that $\phi_\tau u_\tau = q_w/\rho c$, so the Stanton number can be conveniently rewritten as a function of the friction parameters:

$$St = \frac{\alpha \left|\frac{\partial \phi}{\partial y}\right|_{y=0}}{U_{ref}(T_w - T_{ref})} = \frac{\phi_\tau u_\tau}{U_{ref}(T_w - T_{ref})} \tag{2.21}$$

Physically, the Stanton number is a measure of the heat flux performed with respect to the capacity of the flow to transport heat.
Another important parameter is the Nusselt number Nu that is a dimensionless quantity used in convective heat transfer, in particular is the ratio of convective to conductive heat transfer, so in general:

$$Nu = \frac{Q_{convection}}{Q_{conduction}} = \frac{h_{conv} A \Delta T}{\frac{\lambda A \Delta T}{L}} = \frac{h_{conv} L}{\lambda} \tag{2.22}$$

where h_{conv} is the convective heat transfer coefficient, λ is the thermal conductivity of the fluid and L is a characteristic length.
It is possible to express the Nusselt number as a function of the Stanton number, Reynolds number and Prandtl number by using the definition of the convective heat transfer coefficient h_{conv}:

$$h_{conv} = \frac{q_w}{T_w - T_{ref}} \tag{2.23}$$

From the Eq. (2.19) the wall heat flux can be expressed as:

$$q_w = St\rho c U_{ref}(T_w - T_{ref}) \tag{2.24}$$

Substituting the Eq. (2.24) into the Eq. (2.23) and remembering that $\lambda = \alpha\rho c$ into Eq. (2.22) yields:

$$Nu = \frac{h_{conv}L}{\lambda} = \frac{St\rho c U_{ref}\left(T_w - T_{ref}\right)L}{\lambda\left(T_w - T_{ref}\right)} = St\frac{U_{ref}L}{\alpha} \tag{2.25}$$

Finally, multiplying and dividing by ν and recalling the definition of the Reynolds number Eq. (1.6) and Prandtl number Eq. (2.2) yields:

$$Nu = StRePr \tag{2.26}$$

2.7 Reynolds analogy

The Reynolds analogy is a theoretical relationship between turbulent momentum and heat transfer based on the mixing length theory. When the Prandtl number:

$$Pr = \frac{\nu}{\alpha} = 1 \tag{2.27}$$

the Reynolds analogy results in a simple relationship between the skin friction coefficient C_f and the Stanton number St:

$$2St = C_f \tag{2.28}$$

Mathematically, the streamwise velocity component and temperature have the same solution, if their governing equations, boundary conditions and initial conditions are all identical.
In practical applications, this relationship is rarely exact because the Prandtl number differs from unity ($Pr \neq 1$). Consequently, diffusion effects manifest differently within the momentum and energy equations.
Therefore, it is possible to introduce a Reynolds analogy factor A_{fact} defined as:

$$A_{fact} = \frac{2St}{C_f} \tag{2.29}$$

which quantifies the deviation from the Reynolds analogy.

Chapter 3

Turbulent flow control

For decades, considerable research efforts have therefore been devoted to the development of flow-control techniques capable of modifying turbulent structures in order to improve the overall performance of fluid systems. Depending on the desired application, the objective may consist of reducing friction drag, increasing heat-transfer efficiency, suppressing flow separation, reducing aerodynamic noise or enhancing scalar mixing. Since these transport phenomena are all governed by the same turbulent motions, manipulating turbulence offers the possibility of simultaneously affecting several engineering quantities.

Flow-control techniques are generally classified into two main categories: passive and active control.

Passive control relies on fixed geometrical modifications that require no external energy input. Typical examples include riblets, rough surfaces, vortex generators and specially designed wall textures. These devices alter the turbulent flow through purely geometrical effects and are generally simple to implement. However, their performance is usually optimized for a limited operating condition and cannot adapt to changing flow regimes.

Active flow control, instead, introduces an external forcing into the flow in order to modify the turbulent dynamics. The forcing may consist of wall motion, blowing and suction, synthetic jets, plasma actuators, electromagnetic forcing or localized body forces. Unlike passive devices, active control can be adjusted during operation by varying its amplitude, frequency or spatial distribution, allowing greater flexibility and potentially larger performance improvements.

A second important distinction concerns the control strategy itself. Active techniques can be either closed-loop or open-loop. In closed-loop control, the actuation continuously depends on measurements provided by sensors distributed throughout the flow. The controller processes the measured information and determines the appropriate forcing in real time, allowing the system to react to instantaneous changes in the turbulent structures. Although this approach is theoretically capable of achieving optimal performance, its practical implementation remains extremely challenging because of the high dimensionality and chaotic nature of turbulent flows, as well as the demanding sensing and computational requirements.

Open-loop control, on the other hand, prescribes the forcing independently of the instantaneous flow field. The actuation follows a predefined temporal or spatial law

that is selected according to previous theoretical, numerical or experimental investigations. Despite its apparent simplicity, open-loop strategies have demonstrated remarkable effectiveness in wall turbulence, especially when the forcing parameters are properly tuned to interact with the characteristic time and length scales of the near-wall turbulence regeneration cycle. Their simplicity, robustness and relatively low implementation cost make open-loop techniques particularly attractive for practical engineering applications.
The principal passive techniques exploit surface modifications such as riblets, small streamwise-aligned grooves capable of reducing drag by altering the near-wall structures; however, their performance is generally modest and strongly dependent on the specific flow conditions, which limits their robustness outside the design point.
The most common active control techniques include wall blowing and suction, which can be used to manipulate the near-wall turbulence structures, and spanwise forcing, which has two main variants: spanwise wall oscillation and spanwise travelling waves. These techniques are designed to disrupt the self-sustaining cycle of near-wall turbulence, leading to drag reduction and modulation of heat transfer.

3.1 Spanwise wall oscillation

Among the various open-loop control techniques, spanwise wall oscillation stands out as one of the most effective and widely investigated strategies for manipulating wall-bounded turbulent flows. The pioneering numerical study was performed by Jung et al. [6], who conducted a Direct Numerical Simulation (DNS) of a plane channel flow subjected to a spanwise oscillating wall, where the wall velocity is prescribed as:

$$w_w(t) = A\sin(\omega t) \tag{3.1}$$

This strategy is fully characterized by two control parameters: the oscillation amplitude A and the oscillation frequency ω (or equivalently, the oscillation period $T = 2\pi/\omega$).
The physical effect of spanwise wall oscillation is the generation of a *Stokes layer* in the near-wall region, i.e. a thin, time-dependent layer of fluid that oscillates in response to the periodic wall motion, with a wall-normal thickness $\delta_{St} \propto \sqrt{\nu T}$ that grows with the oscillation period. As this transverse boundary layer develops, it disrupts the spatial coherence and phase alignment between quasi-streamwise vortices and streamwise velocity streaks, introduced in Section 1.5. By weakening this self-sustaining cycle, the forcing leads to a significant reduction of turbulent momentum transport and of the Reynolds shear stresses near the wall.

3.2 Drag reduction

The macroscopic consequence of disrupting near-wall coherent structures through spanwise forcing is a significant reduction in the mean skin-friction drag. To quantify the performance of the control strategy, the drag reduction rate (DR) is introduced, typically expressed in percentage form:

$$DR[\%] = \frac{C_{f,0} - C_f}{C_{f,0}} \times 100 \tag{3.2}$$

where $C_{f,0}$ is the skin-friction coefficient of the uncontrolled flow and C_f is the skin-friction coefficient of the controlled flow.
Remebering the skin-friction coefficient Eq. (1.20), where in the channel flow the reference velocity is the bulk velocity U_b. When the flow is driven by a constant pressure gradient (CPG), the drag reduction rate is due to the increase of the mass flow rate, and the drag reduction can be expressed as a function of the bulk velocity:

$$DR[\%] = \frac{U_b^2 - U_{b,0}^2}{U_b^2} \times 100 \tag{3.3}$$

3.3 Heat transfer reduction

In close analogy with momentum transport manipulation, open-loop active control via spanwise wall forcing significantly alters the thermal transport properties of the flow. To quantify the variations in thermal efficiency, the Heat Transfer Reduction rate (HR) is defined based on the Nusselt number (Nu) or the Stanton number (St) of the controlled and uncontrolled flows:

$$HR[\%] = \frac{Nu_0 - Nu}{Nu_0} \times 100 = \frac{St_0 - St}{St_0} \times 100 \tag{3.4}$$

where the subscript 0 denotes the unactuated baseline flow. The physical mechanism underlying the reduction of heat transfer is rooted in the modification of the near-wall coherent thermal structures. The generalized laminar Stokes layer generated by the wall oscillation introduces a periodic transverse shear that skews and disrupts the thermal streaks, which are tightly coupled to the velocity streaks. This spatial disruption weakens the turbulent wall-normal scalar flux $\langle \phi' u_y' \rangle$, effectively thickening the conductive sublayer and reducing the overall efficiency of turbulent convection.

3.4 Dissimilar control

In wall-bounded turbulent flows, momentum and heat transfer are typically highly correlated phenomena. This strong coupling is traditionally described by the Reynolds analogy, which implies that any modification to the flow field aimed at reducing skin friction inherently results in a proportional reduction in convective heat transfer. However, in many engineering applications—such as thermal management systems, advanced heat exchangers, or the cooling of gas turbine blades—this coupled behavior is detrimental. In such scenarios, it is highly desirable to reduce aerodynamic drag without severely deteriorating the heat transfer, or conversely, to enhance heat transfer without incurring an excessive penalty in pumping power.
The concept of *dissimilar control* refers specifically to the ability to manipulate the

turbulent flow field in order to decouple these two transport mechanisms. Achieving dissimilar control fundamentally requires breaking the Reynolds analogy. This is generally accomplished by introducing active or passive flow control strategies designed to interact differently with the kinematic and thermal fields. The primary objective is to selectively alter the turbulent structures that dominate the momentum flux, such as near-wall vortices, while independently modulating or preserving the mechanisms responsible for the turbulent wall-normal heat flux. By doing so, it becomes possible to manage skin friction and heat transfer independently, overcoming the inherent limitations of standard turbulent boundary layers.

Chapter 4

Numerical flow set-up

4.1 Physical modelling

The problem under investigation is a fully developed turbulent channel flow at a friction Reynolds number Re_{τ},, where temperature is treated as a passive scalar advected and diffused by the flow. The dimensional governing equations for an incompressible fluid with constant properties ρ, ν, α are the continuity, Navier–Stokes and energy equations:

$$\begin{cases} \dfrac{\partial u_i}{\partial x_i} = 0 \\ \dfrac{\partial u_i}{\partial t} + \dfrac{\partial (u_i u_j)}{\partial x_j} = -\dfrac{1}{\rho}\dfrac{\partial p}{\partial x_i} + \nu \dfrac{\partial^2 u_i}{\partial x_j \partial x_j} \\ \dfrac{\partial T}{\partial t} + \dfrac{\partial (T u_i)}{\partial x_i} = \alpha \dfrac{\partial^2 T}{\partial x_i \partial x_i} \end{cases} \tag{4.1}$$

Eqs. (4.1) are posed on an infinite channel, but a DNS domain is finite and periodic in x and z. In a physically developing channel flow, however, neither p nor T is periodic in x: a constant streamwise pressure gradient is required to balance the wall shear stress, and a constant streamwise temperature gradient is required to balance the wall heat flux. To recover periodicity, both fields are split into a linear, x-only "driving" part and a periodic residual:

$$p(x, y, z, t) = p^*(x, y, z, t) + \left(\frac{dP}{dx}\right) x \tag{4.2}$$

$$T(x, y, z, t) = \phi(x, y, z, t) + \left(\frac{dT_b}{dx}\right) x \tag{4.3}$$

where p^* and ϕ are periodic in x and z, and dP/dx, dT_b/dx are constants (with their own physical sign: $dP/dx < 0$ for a flow driven in the positive x direction, and $dT_b/dx > 0$ for a fluid being heated as it flows downstream).
Substituting the pressure decomposition into the momentum equation, and using $\partial p/\partial x_i = (dP/dx)\,\delta_{i1} + \partial p^*/\partial x_i$, gives directly

$$\frac{\partial u_i}{\partial t} + \frac{\partial (u_i u_j)}{\partial x_j} = -\frac{1}{\rho}\frac{\partial p^*}{\partial x_i} + \nu \frac{\partial^2 u_i}{\partial x_j \partial x_j} - \frac{1}{\rho}\frac{dP}{dx}\hat{x} \tag{4.4}$$

Since $dP/dx < 0$, the last term is a positive streamwise forcing, as required to sustain the flow against friction.
Substituting the temperature decomposition into the energy equation requires one additional step, because the advection term is nonlinear in T. Writing $G \equiv dT_b/dx$ for brevity and using $T = Gx + \phi$:

$$\frac{\partial T}{\partial t} = \frac{\partial \phi}{\partial t} \tag{4.5}$$
$$\frac{\partial (T u_i)}{\partial x_i} = \frac{\partial (\phi u_i)}{\partial x_i} + Gu \tag{4.6}$$
$$\frac{\partial^2 T}{\partial x_i \partial x_i} = \frac{\partial^2 \phi}{\partial x_i \partial x_i} \tag{4.7}$$

where the advection term was expanded using the product rule; the incompressibility constraint $\partial u_i/\partial x_i = 0$ eliminates one of the two resulting terms, leaving only the streamwise velocity component u multiplying G. The Laplacian of the linear term Gx vanishes identically, since Gx is linear in x. Collecting terms:

$$\frac{\partial \phi}{\partial t} + \frac{\partial (\phi u_i)}{\partial x_i} + G\,u = \alpha \frac{\partial^2 \phi}{\partial x_i \partial x_i} \tag{4.8}$$

The term Gu is the thermal analogue of the pressure-forcing term above: it is not an external heat source, but the bookkeeping term that restores periodicity once the mean streamwise temperature growth has been factored out. It is present regardless of Pr or of any wall control, and it must balance, in the mean, the total heat extracted through the two walls.
Finally, the streamwise pressure and temperature gradients are fixed, respectively, by a force balance and by a global energy balance on the two heated walls:

$$\frac{dP}{dx} = -\frac{\rho u_\tau^2}{h} \tag{4.9}$$
$$\frac{dT_b}{dx} = \frac{q_w}{\rho c_p\, h\, U_b} \tag{4.10}$$

4.2 Non-dimensionalization of the governing equations

The equations are scaled using the channel half-height h, the friction velocity u_τ, the reference time $t_{ref} = h/u_\tau$, and the friction temperature ϕ_τ, defined as

$$\phi_\tau \equiv \frac{q_w}{\rho c_p\, u_\tau}, \tag{4.11}$$

the thermal analogue of u_τ. The non-dimensional variables are

$$u_i^+ = \frac{u_i}{u_\tau} \qquad x_i^+ = \frac{x_i}{h} \qquad t^+ = \frac{t}{t_{ref}} \qquad p^{*+} = \frac{p^*}{\rho u_\tau^2} \qquad \phi^+ = \frac{\phi}{\phi_\tau} \tag{4.12}$$

Substituting into the momentum equation and introducing the friction Reynolds number Re_τ Eq. (1.23) gives directly

$$\frac{\partial u_i^+}{\partial t^+} + \frac{\partial (u_i^+ u_j^+)}{\partial x_j^+} = -\frac{\partial p^{*+}}{\partial x_i^+} + \frac{1}{Re_\tau} \frac{\partial^2 u_i^+}{\partial x_j^+ \partial x_j^+} + \hat{x} \tag{4.13}$$

For the energy equation Eq. (4.8), the forcing term needs to be expressed in non-dimensional form using the energy balance Eq. (4.10) and the definition of ϕ_τ:

$$G\, h\, u_\tau \cdot \frac{u^+}{\phi_\tau} \;=\; \frac{q_w}{\rho c_p\, U_b} \cdot \frac{h\, u_\tau}{\phi_\tau} \cdot u^+ \;=\; \frac{u_\tau}{U_b}\, u^+ \;=\; \frac{u^+}{U_b^+} \tag{4.14}$$

where $U_b^+ = U_b/u_\tau$. This is precisely why ϕ_τ must be defined as $q_w/(\rho c_p u_\tau)$: any other choice would not produce the clean u^+/U_b^+ form. Introducing also the Prandtl number $Pr = \nu/\alpha$, the non-dimensional energy equation becomes

$$\frac{\partial \phi^+}{\partial t^+} + \frac{\partial (\phi^+ u_i^+)}{\partial x_i^+} + \frac{u^+}{U_b^+} = \frac{1}{Re_\tau Pr} \frac{\partial^2 \phi^+}{\partial x_i^+ \partial x_i^+} \tag{4.15}$$

The unit vector $\hat{x}$ in the momentum equation and the term u^+/U_b^+ in the energy equation play the same role: both restore, in a periodic domain, the constant driving gradients that a real (spatially developing) channel flow would otherwise establish naturally.

4.3 Boundary conditions

For the baseline (unactuated) case, no-slip and no-penetration conditions are enforced at both walls ($y = 0$ and $y = 2h$), with periodic boundary conditions in x and z:

$$U = 0, \qquad V = 0, \qquad W = 0. \tag{4.16}$$

The periodic scalar ϕ^+ can be further decomposed into a wall-normal mean profile and an instantaneous fluctuation,

$$\phi^+(x, y, z, t) = \Phi^+(y) + \phi^{+\prime}(x, y, z, t) \tag{4.17}$$

Two physically distinct statements are hidden in this decomposition, and it is important to keep them separate. When decomposing ϕ^+ into a mean and a fluctuating component according to Eq. (4.1), the mean profile must satisfy $\Phi^+(y = 0, 2h) = 0$ by construction, since the mean streamwise growth has already been absorbed into Gx. The condition on the fluctuation $\phi^{+\prime}$ is instead a modelling choice for the wall thermal boundary condition, representing a limiting case of the conjugate heat transfer problem between fluid and wall (Tiselj et al. 2001): a non-fluctuating condition $\phi^{+\prime} = 0$ for a thermally rigid wall, or a fluctuating condition $\partial\phi^{+\prime}/\partial y = 0$ for a thermally compliant wall.
Imposing $\phi^+ = 0$ pointwise at the wall enforces both conditions at once, and is equivalent to the non-fluctuating case. This isothermal condition, adopted here and implemented in Incompact3d, matches Kim & Moin (1989), Kasagi et al. (1992)

and Tiselj (2014), allowing direct comparison with these reference datasets.
Accordingly, the non-dimensional temperature fluctuation is set to zero at both walls:

$$\Phi = 0, \qquad \phi^{+\prime} = 0 \qquad \text{at } y = 0 \text{ and } y = 2h, \tag{4.18}$$

with periodic boundary conditions in x and z.

4.4 Control technique: Spanwise wall oscillation

This study compares the fixed-wall baseline with a controlled case featuring spanwise wall oscillations:

$$w_w = A \sin\left(\frac{2\pi}{T} t\right). \tag{4.19}$$

The control parameters are the amplitude A^+ and the period T^+, defined in viscous units as

$$A^+ = \frac{A}{u_\tau} \qquad T^+ = \frac{T u_\tau^2}{\nu}. \tag{4.20}$$

In this configuration, the velocity boundary conditions at both walls become

$$U = 0, \qquad V = 0, \qquad W = A \sin(\omega t), \tag{4.21}$$

with periodic conditions maintained in x and z. The boundary conditions for the temperature field remain identical to the fixed-wall case, $\Phi = 0$ and $\phi^{+\prime} = 0$ at both $y = 0$ and $y = 2h$, with periodic conditions in x and z.

4.5 Computational domain and simulation cases

The computational domain is the same for the simulation with fixed walls and oscillating walls. Each simulation runs with two passive scalars, with different Prandtl number $Pr = 0.71$ (air) and $Pr = 0.025$ (liquid metal). See Table 4.1 for the dimension of domain and the grid resolution.
In this work, the turbulent channel flow is driven utilizing a Constant Pressure Gradient (CPG) configuration. Under this formulation, the mean pressure gradient forcing the fluid in the streamwise direction is kept strictly invariant throughout the entire simulation. A fundamental implication of this approach concerns the treatment of the friction velocity, $u_\tau = \sqrt{\tau_w/\rho}$. Rather than assigning a fixed default value, u_τ is treated as a variable determined by the active physics of the simulation and properly scaled according to the CPG constraints. At a statistically steady state, the mean wall shear stress τ_w must perfectly balance the constant driving pressure force. When the spanwise wall oscillation is activated and drag reduction occurs, the fixed pressure gradient causes a global acceleration of the core flow, resulting in an upward shift of the bulk velocity (U_b), while u_τ remains inherently anchored to the physical driving force of the system.
In the case of oscillating walls, the amplitude of the wall oscillation in viscous units is $A^+ = 12$ and the period is $T^+ = 100$. The choice of these parameters is based on the literature.

Dataset	Re_τ	L_x	L_z	$N_x \times N_y \times N_z$	$\Delta x^+, \Delta y^+, \Delta z^+$	Δt
Fw	180	$12h$	$6h$	$270 \times 257 \times 270$	$8.0, 0.487 - 4.0, 4.0$	0.01
Ow	180	$12h$	$6h$	$270 \times 257 \times 270$	$7.985, 0.485 - 4.0, 3.992$	0.01

Table 4.1: Summary of the numerical set-up for all simulations.

4.6 Numerical procedure

The present Direct Numerical Simulations (DNS) of turbulent channel flow are performed using Incompact3d (Laizet & Lamballais (2009) [9]). Originally developed to bridge the gap between fully spectral Navier–Stokes solvers and versatile but lower-order finite-difference codes, Incompact3d provides quasi-spectral accuracy while maintaining the simplicity and efficiency of a Cartesian mesh implementation.
The solver integrates the incompressible Navier–Stokes equations alongside the passive scalar transport equation for the temperature field. Spatial discretization relies on high-order compact finite-difference schemes. Specifically, a sixth-order compact scheme is applied to evaluate the first and second derivatives for both the convective and diffusive terms. To ensure numerical stability and energy conservation, the convective terms are cast in a skew-symmetric form, which effectively reduces aliasing errors.
Time advancement is achieved through a fractional-step method. The diffusive terms are integrated implicitly using a second-order Crank–Nicolson (CN) scheme, whereas a third-order Runge–Kutta (RK3) explicit scheme is utilized for the convective terms.
A key feature of the numerical procedure is its treatment of the incompressibility constraint. The Poisson equation for the pressure is formulated and solved directly in spectral space using 3D Fast Fourier Transforms (FFT). This spectral equivalence approach allows the divergence-free condition to be enforced up to machine accuracy. Furthermore, to suppress non-physical spurious pressure oscillations, the code employs a partially staggered mesh arrangement, where the pressure nodes are shifted by a half-mesh spacing relative to the collocated velocity nodes.

4.7 Validation of the code

The numerical code has been validated against the reference dataset of Tiselj et al. (2014) [15] for a turbulent channel flow at $Re_\tau = 180$ with a passive scalar at low Prandtl number $Pr = 0.01$.

Dataset	Lx, Ly, Lz	$Nx \times Ny \times Nz$	$\Delta x^+, \Delta z^+$	Δ_y^+	Δt
Validation	$8h, 2h, 4h$	$128 \times 257 \times 128$	$11.2, 5.64$	$0.5 - 3.96$	0.01
Tiselj et al. (2014)	$12.57h, 2h, 4.2h$	$128 \times 129 \times 128$	$17.7, 5.89$	$0.054 - 4.42$	0.027

Table 4.2: Summary of the numerical set-up for the validation case.

The results obtained for the validation are presented in Fig. 4.1, showing the mean velocity and mean temperature profiles. Both profiles exhibit excellent agreement

with the reference data.
Next, the results for the second-order statistics are analyzed. Fig. 4.2 displays the Reynolds stresses, while Fig. 4.3 shows the temperature RMS fluctuations and the turbulent heat fluxes.
Regarding the temperature statistics, the numerical results exhibit good agreement with the reference dataset as well, thereby confirming the reliability of the solver for the simulation of turbulent flows involving passive scalars at low Prandtl numbers.

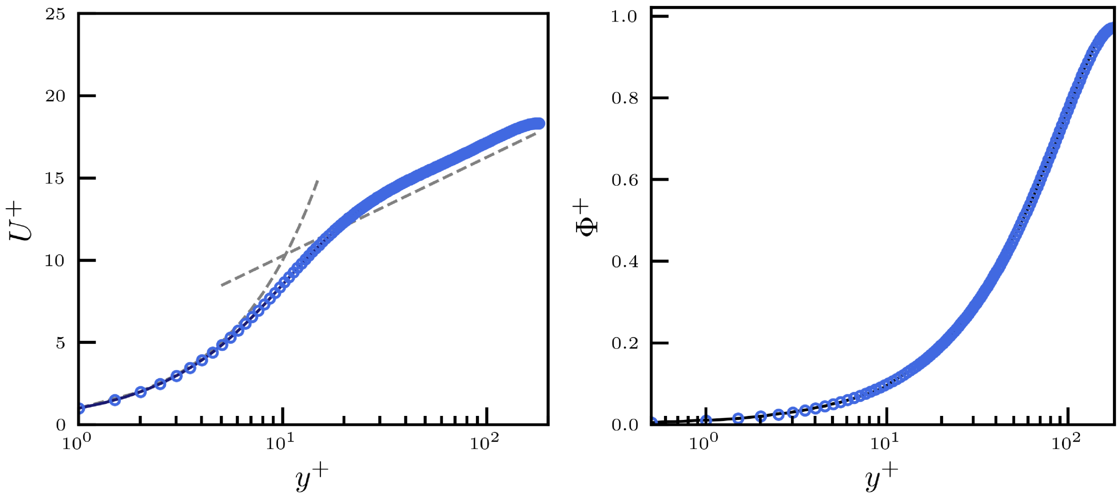

(a) (b)

Figure 4.1: Wall-normal distribution of the mean: (a) streamwise velocity and (b) temperature. Statistics obtained from the present simulation (represented by blue circular markers) are compared with the reference data of Tiselj et al. (2014), which are shown by the dark blue solid line (velocity) and the black solid line (temperature).

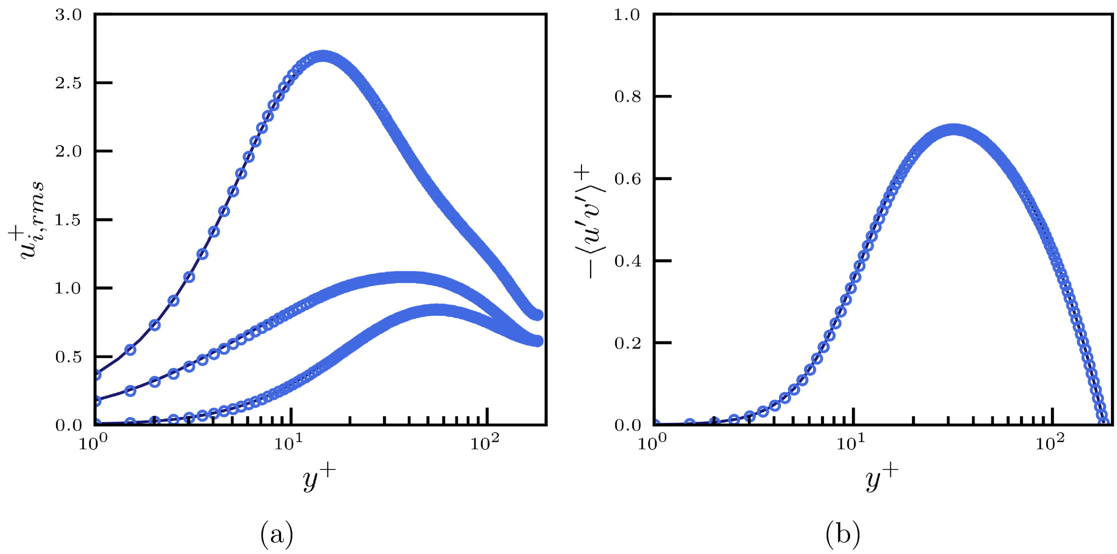

Figure 4.2: Wall-normal distribution of the Reynolds stress components: (a) RMS of the velocity fluctuations and (b) Reynolds stress. See the caption of Fig. 4.1 for the legend.

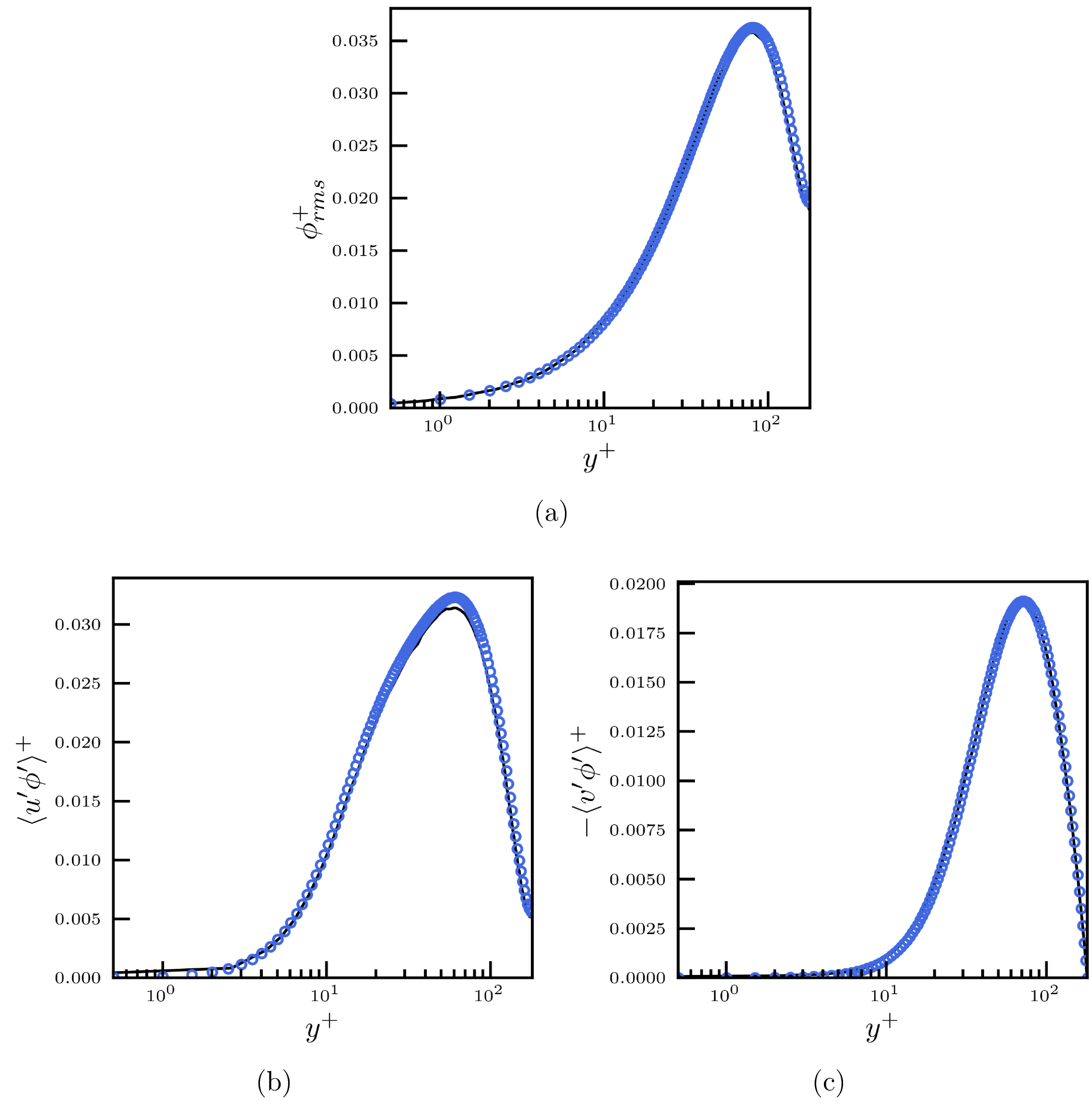

Figure 4.3: Wall-normal distribution of the turbulent heat transport: (a) RMS of the temperature fluctuations, (b) $\langle u'\phi' \rangle^+$ and (c) $\langle v'\phi' \rangle^+$. for $Pr = 0.01$. See the caption of Fig. 4.1 for the legend.

Chapter 5

Results

This chapter presents the results of the simulations

5.1 Global Fluid Dynamic and Heat Transfer Performance

In this section, the macroscopic effects of spanwise wall oscillations are analyzed with particular emphasis on the coupling between momentum and heat transfer. The primary quantities of interest are the skin-friction coefficient (C_f), the Stanton number (St). Classical integral quantities such as drag reduction (DR) and heat transfer reduction (HR) are reported for comparison with existing literature, but are not used as primary descriptors of the flow physics.

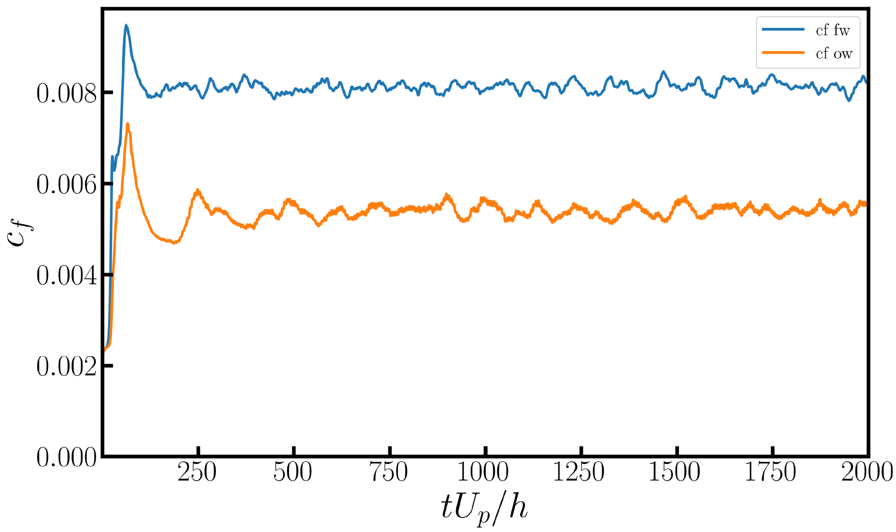

Figure 5.1: Plot of the skin-friction coefficients as a function of time for both unactuated (blue line) and actuated (orange line) cases.

The baseline fluid dynamic behavior is established using the reference unactuated case (Fig. 5.1). After the initial transient, the skin-friction coefficient reaches a statistically stationary state with mean value $C_f \approx 0.008$, in agreement with classical

DNS data for turbulent channel flow at $Re_\tau = 180$, confirming the validity of the numerical setup.
When spanwise wall oscillations are introduced, a transient adjustment phase is observed, followed by a new statistically stationary state characterized by a reduced mean value of $C_f \approx 0.0055$. In the present Constant Pressure Gradient (CPG) framework, this reduction in wall shear stress is accompanied by an increase in bulk velocity. However, in the context of this study, the variation of C_f is primarily interpreted as one contribution to the modification of the momentum-heat transfer coupling, rather than as an isolated performance metric.

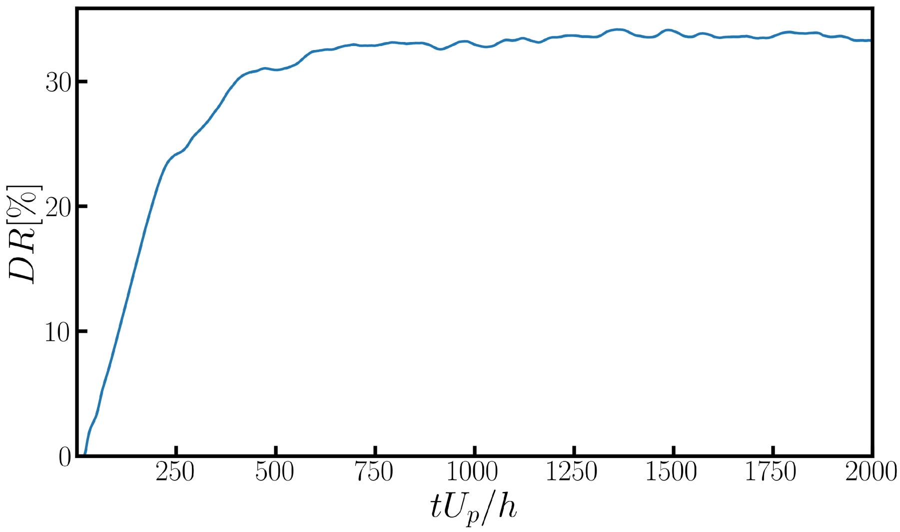

Figure 5.2: Plot of the drag reduction as a function of time

As shown in Fig. 5.2, the drag reduction, evaluated in terms of bulk velocity increase, reaches a statistically steady value of approximately 33%. While this quantity provides a useful global measure for comparison with previous studies, it is not directly used in the present framework, where the focus is placed on the coupled evolution of momentum and heat transfer through C_f and St.
In Fig. 5.3 illustrates the temporal evolution of the wall-oscillation control parameters: the amplitude A^+ (Fig. 5.3a) and the period T^+ (Fig. 5.3b), both expressed in wall units. In both cases, as previously observed for the skin-friction coefficient, the control parameters settle around $A^+ \approx 12$ and $T^+ \approx 100$ following an initial transient phase, successfully recovering the nominal input values selected for the simulation.
The thermal response of the flow is characterized by the Stanton number, whose temporal evolution is reported in Fig. 5.4 for both Prandtl numbers considered. In the unactuated configuration, the Stanton number reaches statistically stationary values of approximately $St \approx 0.004$ for $Pr = 0.71$ and $St \approx 0.039$ for $Pr = 0.025$. Once wall oscillations are applied, a reduction in St is observed in both cases, with final values of $St \approx 0.003$ and $St \approx 0.032$, respectively.
The relative impact of wall forcing on heat transfer is quantified through the heat transfer reduction (HR), defined based on the Stanton number. As shown in Fig. 5.5, for $Pr = 0.71$ the reduction in heat transfer closely follows the reduction in mo-

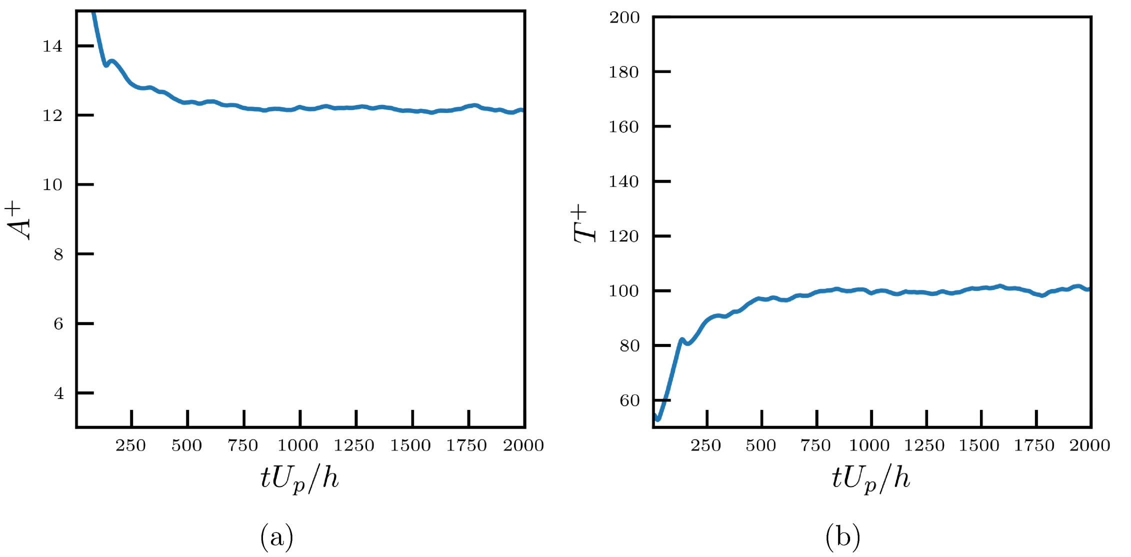

Figure 5.3: Actual inner-scaled oscillation parameters. (a) Amplitude A^+. (b) Period T^+.

mentum transport, with an average value of approximately 33%. In contrast, for $Pr = 0.025$, the reduction is significantly weaker, reaching only about 20%, indicating a partial decoupling between momentum and thermal transport at low Prandtl number Eq. (3.4).
For completeness, the Nusselt number is also reported, computed as

$$Nu = Re_b St Pr \tag{5.1}$$

however, in the present analysis it is treated as a secondary derived quantity, since it includes the effect of bulk velocity variations inherent to the CPG framework. The Stanton number is therefore preferred as the primary descriptor of thermal transport. Fig. 5.6, demonstrates that the Nusselt number for the reference unactuated cases asymptotically stabilizes around an average value of $Nu \approx 18$ for $Pr = 0.71$, whereas it reaches a lower plateau at $Nu \approx 5.4$ for $Pr = 0.025$.
Upon activating the spanwise wall oscillation, a distinct transition phase is observed. For $Pr = 0.71$, the Nusselt number undergoes a permanent reduction, stabilizing around a lower mean value of $Nu \approx 15$. Conversely, for $Pr = 0.025$, the actuated and unactuated curves remain nearly perfectly superimposed throughout the fully developed regime, settling at a mean value of $Nu \approx 5.2$. This direct comparison highlights that while the wall actuation significantly alters the macroscopic thermal performance at moderate Prandtl numbers, its global effect becomes virtually negligible at low Prandtl numbers due to the dominant role of molecular conduction.
A major physical insight emerges from the comparison in Fig. 5.6. While the air case ($Pr = 0.71$) exhibits a substantial heat transfer reduction of approximately 20%, the liquid metal case ($Pr = 0.025$) experiences a marginal reduction restricted to roughly 2%. This stark contrast indicates that at low Prandtl numbers, the global heat transfer performance remains almost entirely unaffected by the wall actuation.
Finally, a remarkable feature of the present dataset is the excellent statistical convergence achieved across all monitored fields. As demonstrated by the long temporal

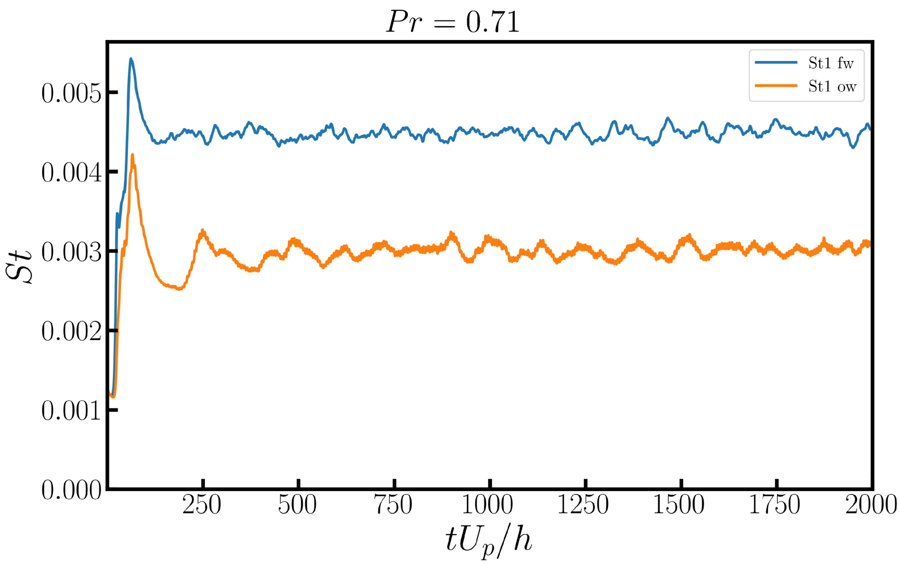

(a)

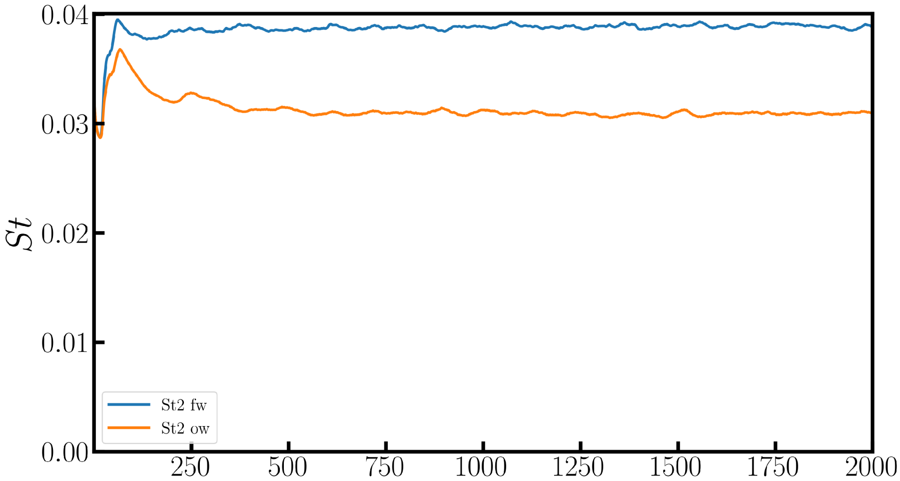

(b)

Figure 5.4: Plot of the Stanton number as a function of time for (a) $Pr = 0.71$ and (b) $Pr = 0.025$. See caption of Fig. 5.1 for legend information.

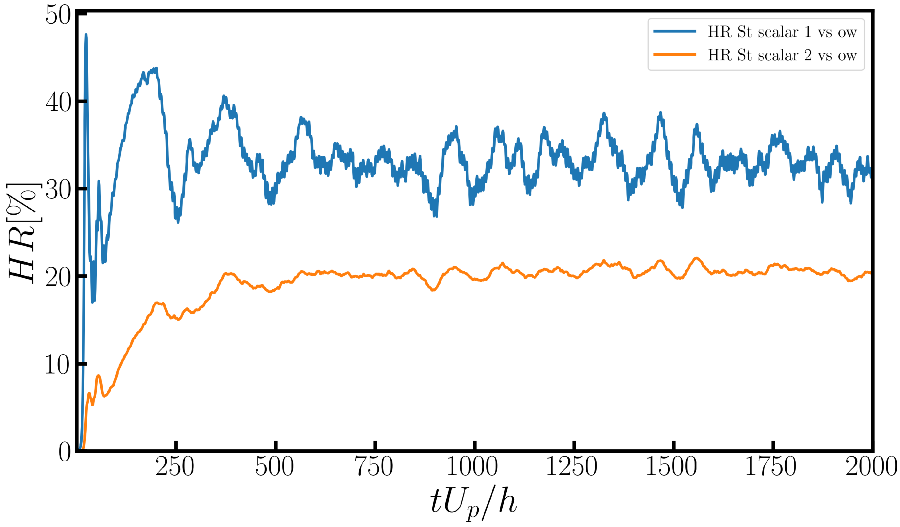

Figure 5.5: Plot of the heat transfer reduction as a function of time for both Prandtl numbers $Pr = 0.71$ (blue line) and $Pr = 0.025$ (orange line).

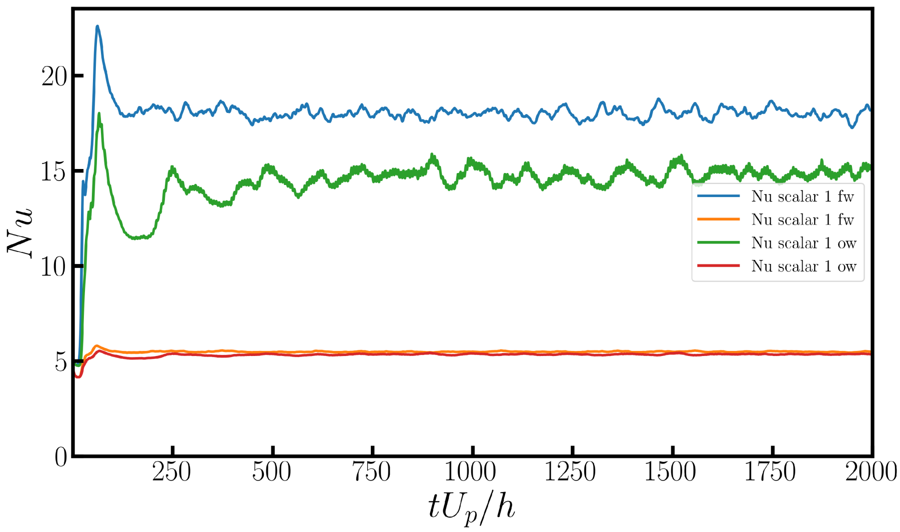

Figure 5.6: Plot of the Nusselt number as a function of time for both unactuated and actuated cases. The Nusselt number is plotted for $Pr = 0.71$ and $Pr = 0.025$.

tracking in Figure 5.4b, the initial transient phase triggered by the activation of the wall control is strictly confined to the earliest stage of the simulation, as clearly demarcated by the shaded transition region. Beyond this threshold, the thermal and fluid dynamic statistics for both $Pr = 0.71$ and $Pr = 0.025$ enter a fully developed, quasi-steady equilibrium, showing only minimal turbulent fluctuations around their respective mean values. This uniform stabilization guarantees that the integration time window selected for statistical averaging is perfectly adequate to completely discard the transient dynamics, ensuring highly reliable and fully converged statistics for the actuated flow regime.

5.2 Effect of Spanwise Wall Oscillations on the Reynolds Analogy

In this section, the influence of spanwise wall oscillations on the validity of the Reynolds analogy is evaluated. Specifically, the deviation from classical Reynolds analogy behavior is quantified using the Reynolds analogy factor (A_{fact}), defined by Eq. (2.29).

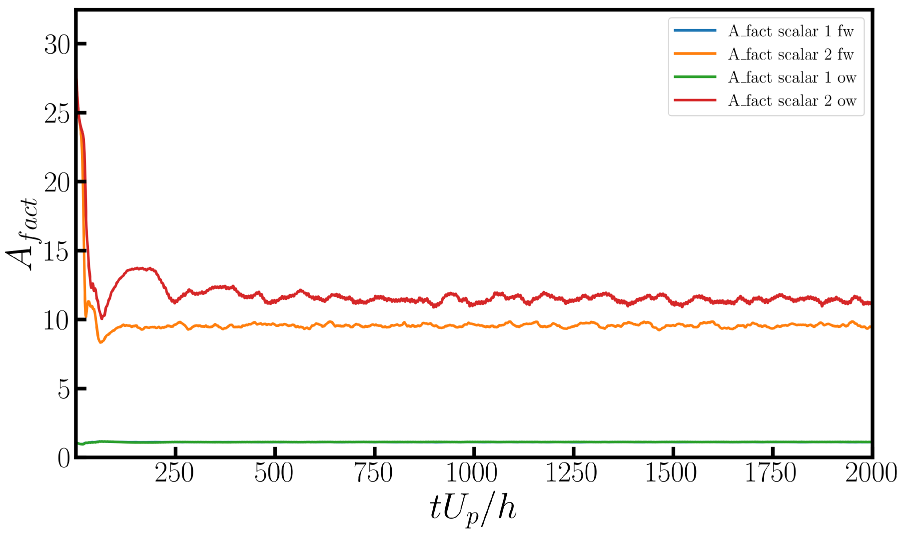

Figure 5.7: Plot of the Reynolds analogy factor as a function of time for both unactuated and actuated cases. The Reynolds analogy factor is plotted for $Pr = 0.71$ and $Pr = 0.025$.

As illustrated in Fig.5.7, the Reynolds analogy factor for $Pr = 0.71$ (blue line and green line) is close to unity ($A_{fact} \approx 1.1$) and exhibits negligible sensitivity to the wall actuation, indicating that the coupling between momentum and thermal transport is closely preserved. Conversely, a profound breakdown of the Reynolds analogy is apparent for fluid at $Pr = 0.025$ across both wall states. In the uncontrolled baseline configuration (orange line), the factor stabilizes at an inherently high value of $A_{fact} \approx 9$. Upon initiating the spanwise wall forcing (red line), an additional distinct decoupling occurs, driving the time-averaged factor to a higher steady-state value around $A_{fact} \approx 11$.

This upward shift in the analogy factor for the low-Prandtl-number case indicates a stronger relative reduction in momentum transport compared to thermal transport under wall forcing.
To better isolate the distinct effects of the active control on thermal versus momentum transport, Fig. 5.8 depicts the fractional change by presenting the ratio of the actuated Reynolds analogy factor to its unactuated baseline counterpart.

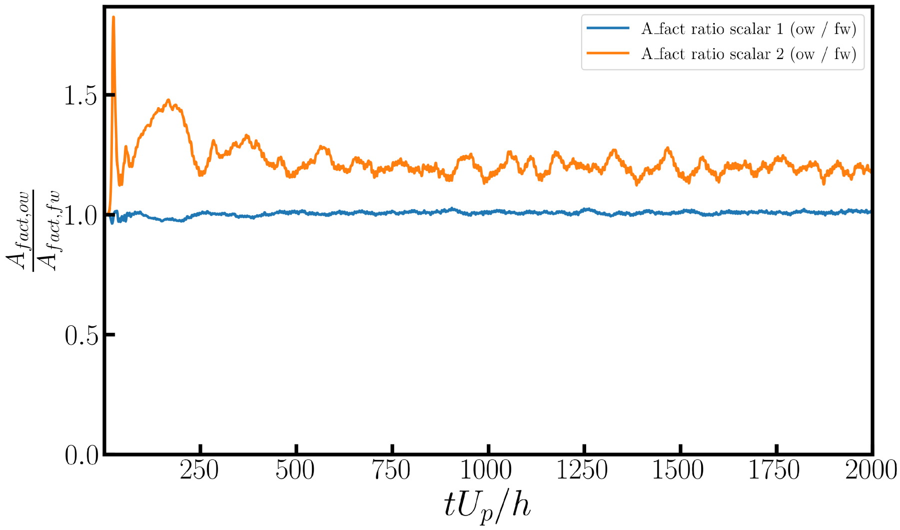

Figure 5.8: Plot of the ratio between the Reynolds analogy factor of the actuated case and the Reynolds analogy factor of the unactuated case for both Prandtl numbers $Pr = 0.71$ (blue line) and $Pr = 0.025$ (orange line).

As shown in Fig. 5.8, the ratio for $Pr = 0.71$ remains virtually equal to unity, reinforcing that standard-Prandtl-number fluids experience an analogous scaling in both friction and thermal transport under control. Conversely, the ratio for $Pr = 0.025$ reaches approximately 1.2. This 20% increase quantitatively demonstrates that spanwise wall forcing introduces a significant dissimilarity in transport mechanisms at low Prandtl numbers, effectively indicating a progressive decoupling between momentum and thermal transport mechanisms induced by spanwise wall forcing at low Prandtl number.

5.3 Mean Profiles and Turbulence Statistics

To gain deeper insight into the local physical mechanisms responsible for the macroscopic changes in drag and heat transfer, the wall-normal distributions of the mean fields and turbulent statistics are investigated. This section analyzes the profiles of the mean velocity $U^+ = U/u_\tau$, the mean temperature $\Phi^+ = \Phi/\phi_\tau$, the turbulent shear stress $\langle u'v' \rangle^+$, and the wall-normal turbulent heat flux $\langle v'\phi' \rangle^+$ for both the reference unactuated (Fw) and actuated (Ow) configurations.
Fig. 5.9 illustrates the mean velocity and temperature profiles for the baseline unactuated case. In the near-wall region, a high degree of similarity is observed between the mean velocity U^+ (Fig.5.9a) and the mean temperature profile for $Pr = 0.71$ (Fig. 5.9b). This close agreement stems directly from the Reynolds analogy, as the

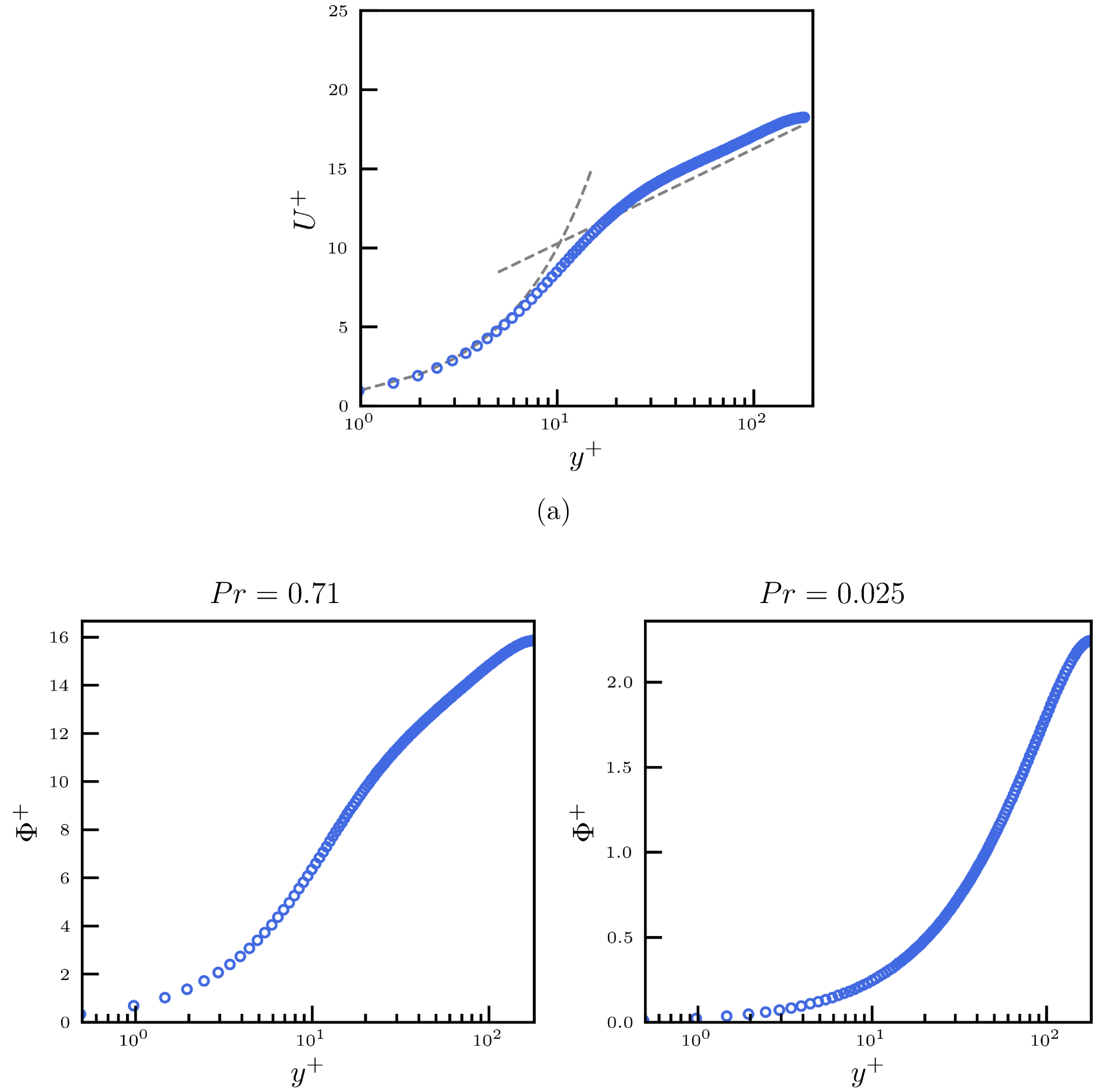

(a) (b) (c)

Figure 5.9: Mean velocity and mean temperature profiles for fixed wall case for $Re_\tau = 180$. (a) Mean velocity profile U^+, (b) Mean temperature profile Φ^+ for $Pr = 0.71$, (c) Mean temperature profile Φ^+ for $Pr = 0.025$.

molecular Prandtl number is close to unity, meaning that momentum and thermal energy diffuse at comparable rates through the viscous sublayer and buffer layer. Conversely, for the low Prandtl number fluid ($Pr = 0.025$, Fig. 5.9c), the mean temperature profile exhibits a prominent downward shift across the entire channel height. This behavior directly reflects the physical mechanisms discussed in the previous chapters: for $Pr < 1$, the conductive range expands because the kinematic viscosity is smaller than the thermal diffusivity ($\nu < \alpha$). This expansion of the conductive range allows molecular conduction to dominate the thermal transport over a much longer distance from the wall, resulting in the characteristic downward shift of the Φ^+ profile throughout the core flow.

The structural impact of the spanwise wall oscillation on the mean fields is summarized in Fig. 5.10. Upon activating the wall control, the mean velocity profile U^+ (Fig.5.10a) experiences a significant upward shift within the logarithmic region. Under the enforced Constant Pressure Gradient (CPG) condition, this upward shift serves as the statistical signature of turbulent drag reduction, reflecting the global acceleration of the core flow due to the suppression of near-wall momentum resistance. For $Pr = 0.71$ (Fig. 5.10b), the mean temperature profile Φ^+ responds to the control with a nearly identical upward shift, demonstrating that the passive scalar field remains strongly coupled to the modified velocity field at moderate Prandtl numbers. A different behavior is observed for $Pr = 0.025$ (Fig. 5.10c). Here, the controlled mean temperature profile shows a negligible upward shift, remaining almost completely superimposed onto the unactuated baseline. This result highlights a profound structural decoupling between momentum and heat transport at low Prandtl numbers under spanwise wall forcing. Because the thickness of the thermal conduction layer is substantially larger than the thin Stokes layer generated by the wall oscillation, the mean thermal field is effectively shielded from the localized mechanical disruption, rendering the global temperature distribution nearly insensitive to the wall actuation.

To analyze the turbulent transport mechanisms, Fig. 5.11 establishes the baseline distributions of the turbulent shear stress $\langle u'v' \rangle^+$ and the wall-normal turbulent heat flux $\langle v'\phi' \rangle^+$ for the reference unactuated flow, while Fig. 5.12 provides the direct comparison with the actuated configuration. The widespread attenuation of the turbulent shear stress $\langle u'v' \rangle^+$ observed in Fig. 5.11a represents the structural cause underpinning the macroscopically observed drag reduction ($DR \approx 32\%$). The spanwise forcing effectively suppresses the cross-stream turbulent mixing responsible for momentum exchange. Crucially, this damping effect extends to the wall-normal turbulent heat flux $\langle v'\phi' \rangle^+$, which is directly linked to the global heat transfer reduction (HR). For $Pr = 0.71$ (Fig. 5.11b), the substantial suppression of the turbulent heat flux restricts the turbulent convective transport, perfectly justifying the 32% drop in the Nusselt number. For the low Prandtl number case ($Pr = 0.025$, Fig. 5.11c), the turbulent heat flux is also visibly damped by the wall control. However, due to the massive contribution of molecular conduction inherent to liquid metals, the turbulent heat flux plays a minor role in the total energy budget within this region. Consequently, even though turbulence is mechanically suppressed by the wall os-

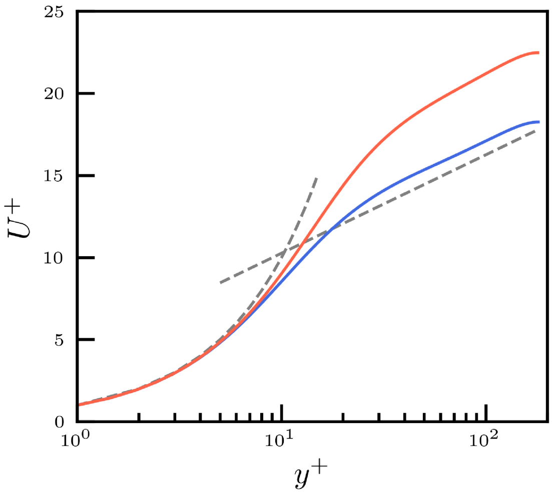

(a)

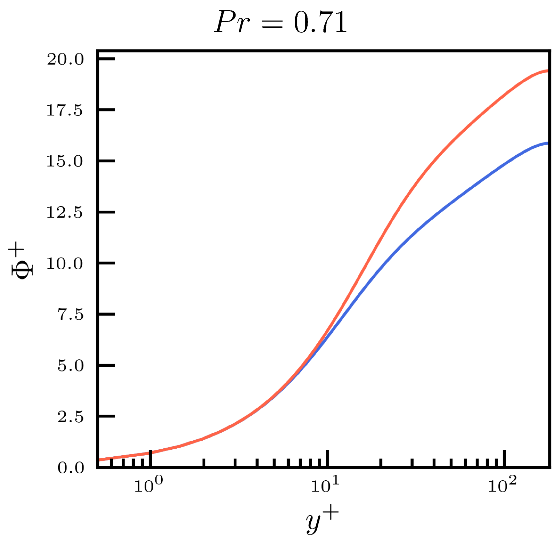

(b)

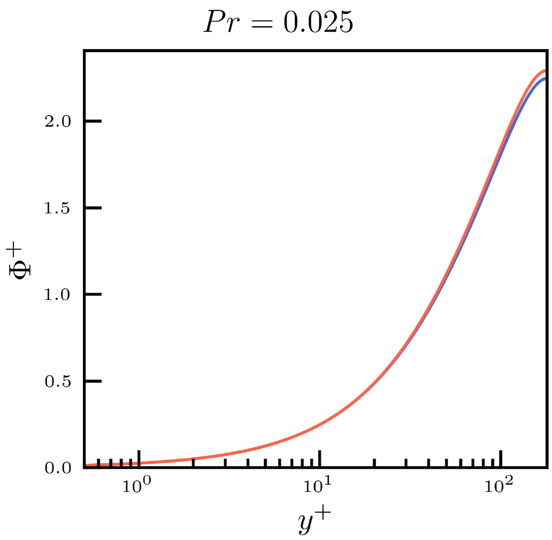

(c)

Figure 5.10: Comparison of the mean velocity and mean temperature profiles between the unactuated (blue line) and actuated cases (orange line) for $Re_\tau = 180$. (a) Mean velocity profile U^+, (b) Mean temperature profile Φ^+ for $Pr = 0.71$, (c) Mean temperature profile Φ^+ for $Pr = 0.025$.

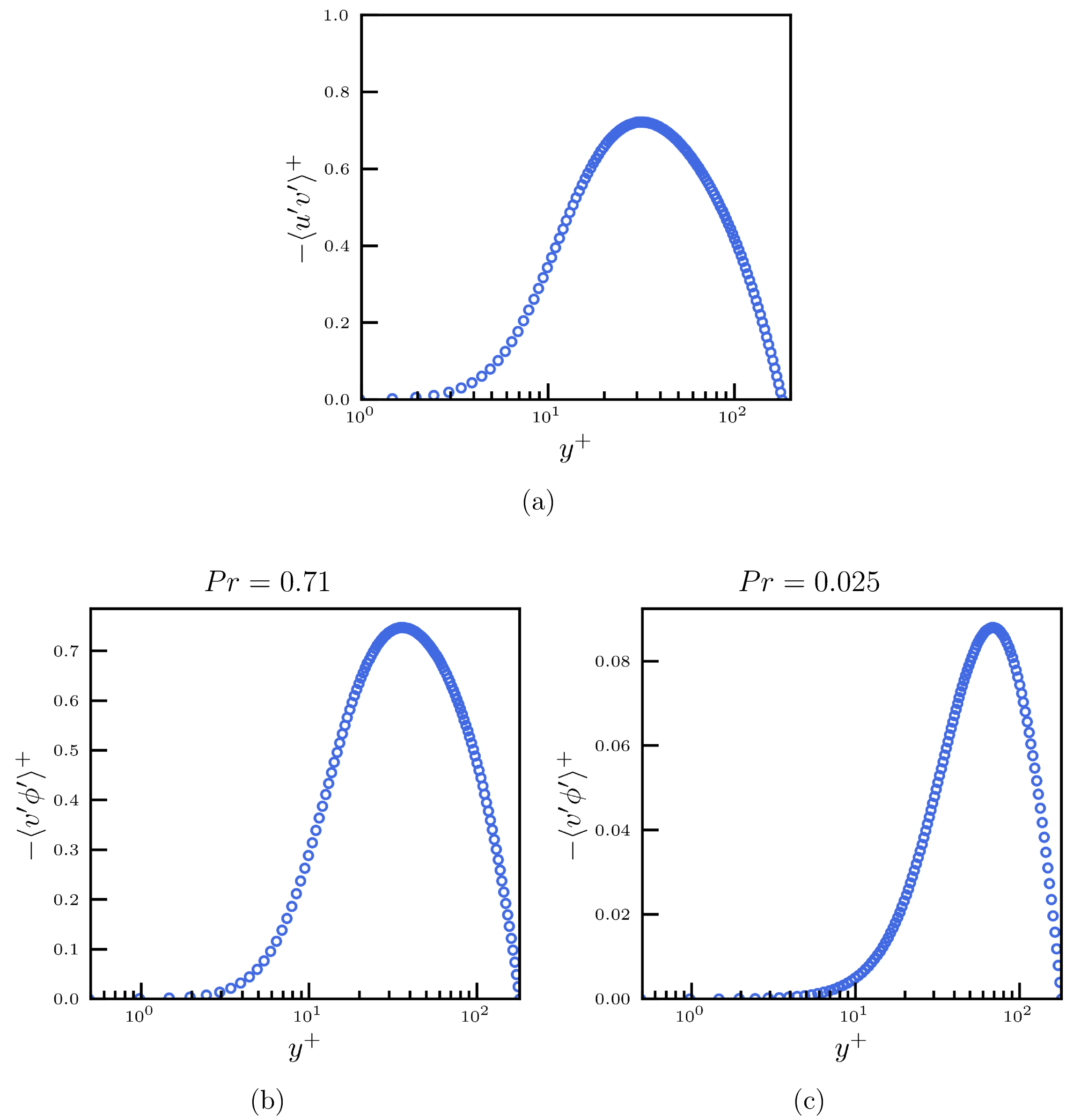

Figure 5.11: Unactuated case: turbulent shear stress $\langle u'v' \rangle^+$ and wall normal turbulent heat flux $\langle v'\phi' \rangle^+$ for $Re_\tau = 180$. (a) Turbulent shear stress, (b) Wall normal turbulent heat flux for $Pr = 0.71$, (c) Wall normal turbulent heat flux for $Pr = 0.025$.

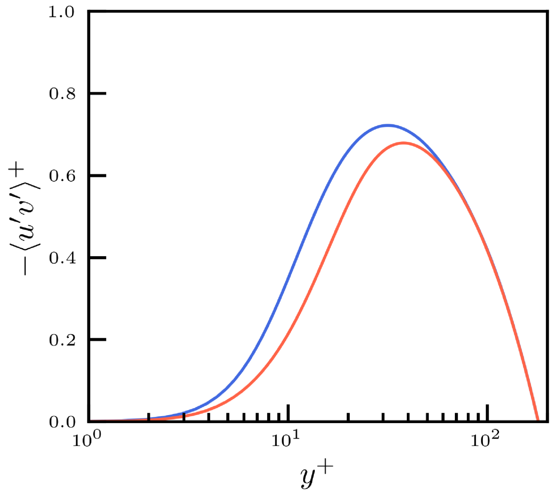

(a)

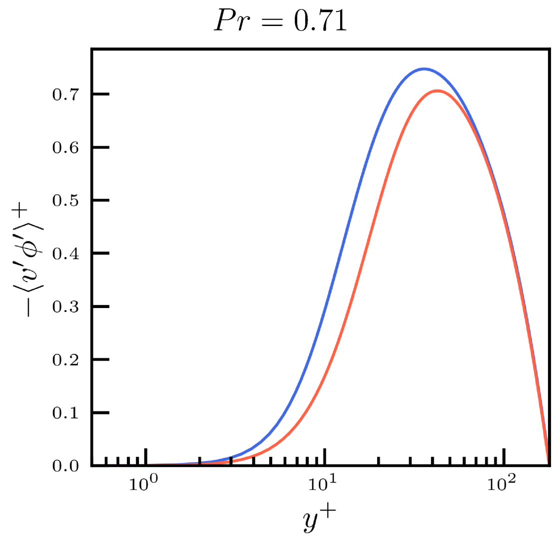

(b)

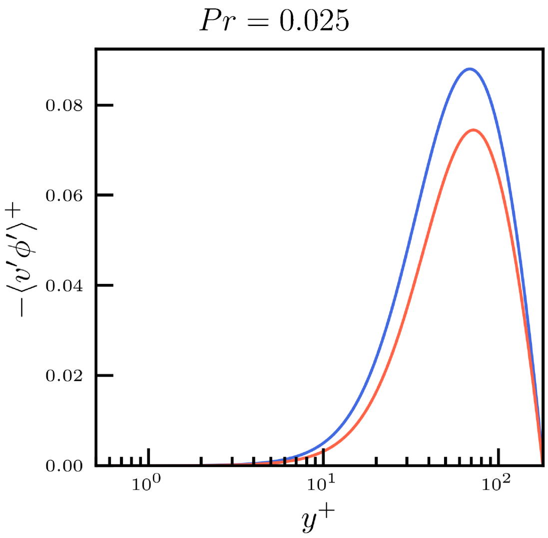

(c)

Figure 5.12: Comparison between the unactuated (blue line) and actuated (orange line) cases of turbulent shear stress $\langle u'v'\rangle^+$ and wall normal turbulent heat flux $\langle v'\phi'\rangle^+$ for $Re_\tau = 180$. (a) Turbulent shear stress, (b) Wall normal turbulent heat flux for $Pr = 0.71$, (c) Wall normal turbulent heat flux for $Pr = 0.025$.

cillation, the total thermal transport remains nearly unaltered, which explains why the global heat transfer reduction is limited to a nearly negligible 20%..

Conclusions

In this work, direct numerical simulations (DNS) of turbulent channel flow with forced convection were performed at a friction Reynolds number of $Re_\tau = 180$. The study investigated the thermal transport characteristics for two distinct Prandtl numbers: $Pr = 0.71$, representative of air, and $Pr = 0.025$, representative of liquid metals. To manipulate the near-wall turbulence, active flow control was applied via spanwise wall forcing, implementing a plane wall oscillation with a fixed amplitude of $A^+ = 12$ and a period of $T^+ = 100$.

The primary focus of this investigation was to evaluate how this active control strategy alters the coupling between momentum and thermal transport, effectively quantified through the Reynolds analogy factor, $A_{fact} = 2St/C_f$. The integration of the present findings into the broader context of recent literature highlights that the behavior of A_{fact} under actuated conditions is strictly dictated by a structural dissimilarity governed by the Prandtl number regime. For fluids with a Prandtl number close to unity ($Pr \approx 1$), previous literature (Guérin et al. 2024) demonstrated that spanwise wall oscillations preserve the Reynolds analogy ($A_{fact} \approx 1$). In that regime, the suppression of near-wall coherent structures—such as low-speed streaks and ejection-sweep events—attenuates drag and heat transfer in a highly synchronized manner, maintaining a cross-correlation between velocity and temperature fluctuations up to 0.90. Conversely, in the high Prandtl number regime ($Pr > 1$), Rouhi (2025) discovered that the Reynolds analogy factor decreases ($A_{fact} < 1$), because the thinning of the conductive sublayer shifts the energetic thermal scales closer to the wall, making them more vulnerable to the damping effects of the Stokes layer than their momentum counterparts.

The results obtained in the present study for the low Prandtl number regime ($Pr = 0.025$) reveal a striking trend reversal that stands in sharp contrast to these previous investigations, marking a profound and favorable breakdown of the Reynolds analogy. Under the effect of spanwise wall oscillations, the skin friction coefficient C_f decreases significantly more than the Stanton number St. Specifically, while the active forcing yields a substantial friction drag reduction of $DR \approx 33\%$, the corresponding heat transfer reduction is notably less pronounced, settling at an average value of $HR \approx 20\%$. Consequently, the Reynolds analogy factor A_{fact} undergoes a distinct increase relative to the unactuated baseline.

This unique phenomenon is physically rooted in the stark asymmetry between the conductive and viscous sublayers characteristic of liquid metals. At Pr=0.025, the thermal field is heavily dominated by molecular conduction over an extended region that reaches far beyond the narrow near-wall zone directly disturbed by the thin viscous Stokes layer. Because the large-scale thermal structures are governed by

high molecular diffusivity, the passive scalar field is largely desensitized to the localized disruption of the quasi-longitudinal vortices and velocity streaks. Therefore, while the control effectively suppresses the turbulent shear stress, its impact on the thermal transport is inherently mitigated. This mechanisms successfully decouples the two transport fields, proving that spanwise wall oscillations can be leveraged to maximize drag reduction in liquid metal applications while effectively optimizing the relative efficiency of the Reynolds analogy factor.
Future developments of this research could, first and foremost, encompass the investigation of different wall oscillation parameters—specifically varying the amplitude A^+ and the period T^+ to evaluate whether alternative forcing configurations could yield further performance enhancements or, conversely, lead to a degradation of the observed effects. Additionally, it would be of great interest to extend this analysis to higher friction Reynolds numbers (Re_τ) to verify whether the behavior documented at $Re_\tau = 180$ persists under more highly turbulent conditions. Furthermore, exploring alternative active flow control strategies, such as spanwise travelling waves, represents another promising avenue for future work. Finally, extending the scope of this investigation from internal channel flows to external configurations, specifically focusing on a flat-plate boundary layer, would provide valuable insights into the broader applicability of these control mechanisms.

Bibliography

[1] Theodore L. Bergman, Adrienne S. Lavine, Frank P. Incropera, and David P. DeWitt. *Fundamentals of Heat and Mass Transfer.* John Wiley & Sons, 8th edition, 2017.

[2] Charles H. Forsberg. *Heat Transfer: Principles and Applications.* Academic Press, 2021.

[3] Marco Galli. Spanwise forcing for turbulent heat transfer enhancement. 2022.

[4] Lou Guérin, Cédric Flageul, Laurent Cordier, Stéphane Grieu, and Lionel Agostini. Preferential enhancement of convective heat transfer over drag via near-wall turbulence manipulation using spanwise wall oscillations. *International Journal of Heat and Fluid Flow*, 110:109564, 2024.

[5] Y Hasegawa and N Kasagi. Dissimilar control of momentum and heat transfer in a fully developed turbulent channel flow. *Journal of Fluid Mechanics*, 683:57–93, 2011.

[6] Wen-Je Jung, Norberto Mangiavacchi, and Rayhaneh Akhavan. Suppression of turbulence in wall-bounded flows by high-frequency spanwise oscillations. *Physics of Fluids A*, 4(8):1605–1607, 1992.

[7] N Kasagi, Y Tomita, and A Kuroda. Direct numerical simulation of passive scalar field in a turbulent channel flow. *Journal of Fluid Mechanics*, 243:1–30, 1992.

[8] John Kim and Parviz Moin. Transport of passive scalars in a turbulent channel flow. In *Turbulent Shear Flows 6: Selected Papers from the Sixth International Symposium on Turbulent Shear Flows, Université Paul Sabatier, Toulouse, France, September 7–9, 1987*, pages 85–96. Springer, 1989.

[9] Sylvain Laizet and Eric Lamballais. High-order compact schemes for incompressible flows: A simple and efficient method with quasi-spectral accuracy. *Journal of Computational Physics*, 228(16):5989–6015, 2009.

[10] Stephen B. Pope. *Turbulent Flows.* Cambridge University Press, 2000.

[11] Maurizio Quadrio and Pierre Ricco. The laminar generalized stokes layer and turbulent drag reduction. *Journal of Fluid Mechanics*, 667:135–157, 2011.

[12] Pierre Ricco, Claudio Ottonelli, Yosuke Hasegawa, and Maurizio Quadrio. Changes in turbulent dissipation in a channel flow with oscillating walls. *Journal of Fluid Mechanics*, 700:77–104, 2012.

[13] Amirreza Rouhi, Marcus Hultmark, and Alexander J Smits. Spanwise wall forcing can reduce turbulent heat transfer more than drag. *Journal of Fluid Mechanics*, 1010:A59, 2025.

[14] Enrico Stalio and Enrico Nobile. Direct numerical simulation of heat transfer over riblets. *International Journal of Heat and Fluid Flow*, 24(3):356–371, 2003.

[15] Iztok Tiselj. Tracking of large-scale structures in turbulent channel with direct numerical simulation of low prandtl number passive scalar. *Physics of Fluids*, 26(12), 2014.